Title
Closed-Form Analytic Solution of Cloud Dissipation for a Mixed-Layer Model

Journal
Journal of the Atmospheric Sciences, 74(8)

ISSN
0022-4928

Authors
Akyurek, Bengu Ozge
Kleissl, Jan

Publication Date
2017-08-01

DOI
10.1175/jas-d-16-0303.1

Peer reviewed

Closed-Form Analytic Solution of Cloud Dissipation for a Mixed Layer Model

Bengu Ozge Akyurek* and Jan Kleissl

Mechanical and Aerospace Engineering, University of California, San Diego

**Corresponding author address:* Bengu Ozge Akyurek, Mechanical and Aerospace Engineering, University of California, San Diego

E-mail: bakyurek@ucsd.edu

ABSTRACT

Stratocumulus clouds play an important role in climate cooling and are hard to predict using global climate and weather forecast models. Thus, previous studies in the literature use observations and numerical simulation tools, such as Large Eddy Simulation (LES), to solve the governing equations for the evolution of stratocumulus clouds. In contrast to the previous works, this work provides an analytic closed-form solution to the cloud thickness evolution of stratocumulus clouds in a mixed layer model framework. With a focus on application over coastal lands, the diurnal cycle of cloud thickness and whether or not clouds dissipate are of particular interest. An analytic solution enables the sensitivity analysis of implicitly interdependent variables and extrema analysis of cloud variables that are hard to achieve using numerical solutions. In this work, the sensitivity of inversion height, cloud base height and cloud thickness with respect to initial and boundary conditions such as Bowen Ratio, subsidence, surface temperature and initial inversion height are studied. A critical initial cloud thickness value that can be dissipated pre and post-sunrise is provided. Furthermore, an extrema analysis is provided to obtain the minima and maxima of the inversion height and cloud thickness within 24 hours. The proposed solution is validated against LES results under the same initial and boundary conditions.

1. Introduction

Stratocumulus clouds (Sc) cover 21% of the earth's surface on average annually and have a relatively high albedo resulting in a cooling contribution to climate (Klein and Hartmann (1993); Eastman and Warren (2014)). Sc also impact Photovoltaic (PV) generation output in coastal areas such as Southern California (Jamaly et al. (2013)). Sc are prevalent over the ocean and the coast line, but less so inland, yet there are also studies focusing on continental Sc (e.g. Kollias and Albrecht (2000)). Their global abundance and the increase in coastal populations make it important to accurately model and forecast their behavior. However, global forecast models fail to accurately represent and forecast Sc (Bony (2005)).

Sc generally form under a strong inversion layer and the resulting boundary layer (BL) is spatially homogeneous and well mixed day and night due to buoyant turbulence forcing from longwave cooling at the cloud top (Lilly (1968); Bretherton and Wyant (1997)). In observational studies, it has been shown that Sc can also form during the day under decoupled conditions, especially for deeper BLs and stronger winds, temperature and moisture gradients, yet they are less prevalent to the well-mixed cases (Serpetzoglou et al. (2008); Rémillard et al. (2012)). Mixed layer models (MLM) are therefore an appropriate tool and have been widely applied to Sc since the groundbreaking work of Lilly (1968). Many studies improved physical model components such as entrainment (Stevens (2002); Fang et al. (2014); Caldwell et al. (2005)), radiation (Larson et al. (2007); Duynkerke (1999)), surface fluxes (Bretherton and Wyant (1997)), and advection (Seager et al. (1995)). MLM are typically numerically integrated, validated against other numerical simulations such as Large Eddy Simulation (LES), and applied to study specific cases or sensitivities in the Sc topped BL (Stevens et al. (2005) and references within). Numerical integration is required due to the fact that the MLM integro-differential equations are often very complex with multiple feedback loops (Ghonima et al. (2016)). However, to understand interdependencies between variables or sensitivity of the system to a parameter, multiple case studies and simulations need to be performed. Even then, hidden interdependencies or feedback effects may not be discovered using trial and error methods.

There are also studies that use analytic models to understand the underlying behaviors (van der Dussen et al. (2014); Duynkerke et al. (2004); Stevens (2002)). However, these studies focus on the modeling of the physical phenomena with better analytic equations, rather than solving the time evolution of cloud variables analytically.

In this work, we build up a physical MLM with radiation, buoyancy flux, and surface schemes and use mathematical approximations to obtain a closed-form analytic solution to inversion height, cloud base height, and ultimately cloud dissipation. The advantage of an analytic solution is that the dependencies and sensitivities are observable directly from equations. For example, and related to our application of solar forecasting over coastal lands, the dependence of cloud thickness on Bowen ratio can be directly inferred, given the initial conditions of the system. The temporal evolution of the system can be described without numerical approximations and steady state conditions or attraction points can be detected.

We provide sensitivity and extrema analysis for inversion height, cloud base height and cloud thickness, to infer how they depend on the initial and boundary conditions, and understand when their minima and maxima occur during the diurnal cycle.

This paper is structured as follows. Section 2 provides a background on the models that constitute the system of equations. In Section 3 the analytic solution is derived. In Section 4, closed-form analytic solution is verified against LES and is shown to closely follow the numerical results. Section 5 contains detailed analysis on the sensitivity of inversion height, cloud base height and cloud thickness evolution in time with respect to the system parameters and initial conditions, and the timing of their extrema during the diurnal cycle.

The radiation and surface models used in this work are similar as in Ghonima et al. (2016), who use numerical time-stepping to solve a similar single-column mixed layer model. Even though the authors show that the MLM results are close to a more complex simulation method (LES), the underlying connections and interdependencies between the cloud variables and the initial conditions are not analyzed. Such an analysis using numerical solution techniques is impractical due to the vast number of variables in the solution space as shown in Figure 2 later, motivating our analytic solution to this problem.

2. Background

In this section, we define the models that approximate the physical processes. Consider a well mixed single vertical column with a single cloud layer bounded by its base height, z_{b}, and the inversion height, z_{i}. An illustration is shown in Figure 1. We assume constant air density ρ_{air} and constant values for the jumps at the inversion layer for total water mixing ratio, $\Delta q_{\mathrm{T,\,i}}$, and liquid potential temperature, $\Delta\theta_{\mathrm{l,\,i}}$, (Lilly (1968)).

The cloud thickness h is the primary parameter of interest and its tendency can be defined as:

$$\frac{dh(t)}{dt} = \frac{dz_{\mathrm{i}}(t)}{dt} - \frac{dz_{\mathrm{b}}(t)}{dt} \tag{1}$$

We use the inversion tendency definition from Caldwell et al. (2005) and Duynkerke et al. (2004), where the inversion height changes with the entrainment parameter, w_{e} and the subsidence, $w_{\mathrm{s}}(z_{\mathrm{i}})$. Subsidence is further approximated by a divergence (Caldwell et al. (2005)):

$$\frac{dz_{\mathrm{i}}}{d_t} = w_{\mathrm{e}}(t) + \mathbf{v}_{\mathrm{H}}\nabla z_{\mathrm{i}} = w_{\mathrm{e}}(t) + w_{\mathrm{s}}(z_{\mathrm{i}}) = w_{\mathrm{e}}(t) + Dz_{\mathrm{i}}(t) \tag{2}$$

The cloud base height tendency expression (Ghonima et al. (2015)) depends on the conserved variables of liquid potential temperature, θ_l and total moisture, q_T:

$$\frac{dz_\mathrm{b}(t)}{dt} = \frac{\mathrm{R_d T_{base}}}{g q_\mathrm{T}(t)} \left(1 - \frac{\mathrm{L_v R_d}}{\mathrm{c_p R_v T_{base}}}\right)^{-1} \frac{dq_\mathrm{T}(t)}{dt} + \frac{\mathrm{c_p}\pi_\mathrm{base}}{g} \left(1 - \frac{\mathrm{c_p R_v T_{base}}}{\mathrm{R_d L_v}}\right)^{-1} \frac{d\theta_\mathrm{l}(t)}{dt} \tag{3}$$

$\mathrm{R_d}$ and $\mathrm{R_v}$ represent the gas constants for dry air and water vapor, respectively, $\mathrm{L_v}$ is the latent heat of evaporation, $\mathrm{c_p}$ is the specific heat, g is the gravitational acceleration, $\mathrm{T_{base}}$ is the temperature at the cloud base, π_base is the Exner function evaluated at the cloud base. In the following sections the inversion height and cloud base height tendencies are derived based on the budget equations for heat and moisture.

a. Budget Equations for Conserved Moisture and Temperature Variables

The MLM budget conservation equations are given for the liquid potential temperature and the total moisture as (Lilly (1968)):

$$\frac{d\theta_\mathrm{l}(t)}{dt} = -\frac{\partial}{\partial z}\left(\overline{\mathrm{w}'\theta_\mathrm{l}'}(z,t) + \frac{\mathrm{F_{rad}}(z,t)}{\mathrm{c_p}\rho_\mathrm{air}}\right) - \theta_\mathrm{l,\,adv}, \qquad \frac{dq_\mathrm{T}(t)}{dt} = -\frac{\partial \overline{\mathrm{w}'q_\mathrm{T}'}(z,t)}{\partial z} - q_\mathrm{T,\,adv} \tag{4}$$

The large scale advection values of total moisture $q_\mathrm{T,\,adv}$ and liquid potential temperature $\theta_\mathrm{l,\,adv}$ are assumed to be zero throughout this work. While advection effects are important for the MBL over coastal lands, the advection terms complicate the integration of the equations and are left for future study. $\overline{\mathrm{w}'\theta_\mathrm{l}'}(z,t)$ and $\overline{\mathrm{w}'q_\mathrm{T}'}(z,t)$ represent the average liquid potential temperature flux and average total moisture flux, respectively. $\mathrm{F_{rad}}$ represents the net radiation flux. Due to the well-mixed assumption, both conserved variables can be assumed to be independent of height. This forces the right hand side of the equations to be also independent of height, resulting in a linear height dependency for the partial derivatives. Representing the partial derivatives as E and W, respectively, we can derive the full expressions using the boundary conditions at $z = 0$ and $z = z_\mathrm{i}$, as given in Bretherton and Wyant (1997):

$$\frac{d\theta_{\mathrm{l}}}{dt} = -\frac{\partial E}{\partial z} \qquad \frac{dq_{\mathrm{T}}}{dt} = -\frac{\partial W}{\partial z} \tag{5}$$

$$E(z) = (1 - z/z_{\mathrm{i}})E(0) + (z/z_{\mathrm{i}})E(z_{\mathrm{i}}) \qquad W(z) = (1 - z/z_{\mathrm{i}})W(0) + (z/z_{\mathrm{i}})W(z_{\mathrm{i}}) \tag{6}$$

The boundary conditions at the surface and inversion height are obtained as:

$$E(0) = \overline{\mathrm{w}'\theta_{\mathrm{l}}'}(0,t) + \mathrm{F}_{\mathrm{rad}}(0,t)/(\rho_{\mathrm{air}}\mathrm{c}_{\mathrm{p}}) \qquad E(z_{\mathrm{i}}) = -w_{\mathrm{e}}\Delta\theta_{\mathrm{l,\,i}} + \mathrm{F}_{\mathrm{rad}}(z_{\mathrm{i}},t)/(\rho_{\mathrm{air}}\mathrm{c}_{\mathrm{p}}) \tag{7}$$

$$W(0) = \overline{\mathrm{w}'q_{\mathrm{T}}'}(0,t) \qquad W(z_{\mathrm{i}}) = -w_{\mathrm{e}}\Delta q_{\mathrm{T,\,i}} \tag{8}$$

The final expressions for θ_{l} and q_{T} tendencies are obtained as:

$$\frac{d\theta_{\mathrm{l}}(t)}{dt} = \frac{\overline{\mathrm{w}'\theta_{\mathrm{l}}'}(0,t)}{z_{\mathrm{i}}(t)} + \frac{\mathrm{F}_{\mathrm{rad}}(0,t)}{\rho_{\mathrm{air}}\mathrm{c}_{\mathrm{p}}z_{\mathrm{i}}(t)} + \frac{w_{\mathrm{e}}(t)\Delta\theta_{\mathrm{l,\,i}}}{z_{\mathrm{i}}(t)} - \frac{\mathrm{F}_{\mathrm{rad}}(z_{\mathrm{i}}(t),t)}{\rho_{\mathrm{air}}\mathrm{c}_{\mathrm{p}}z_{\mathrm{i}}(t)} \tag{9}$$

$$\frac{dq_{\mathrm{T}}(t)}{dt} = \frac{\overline{\mathrm{w}'q_{\mathrm{T}}'}}{z_{\mathrm{i}}(t)} + \frac{w_{\mathrm{e}}(t)\Delta q_{\mathrm{T,\,i}}}{z_{\mathrm{i}}(t)} \tag{10}$$

b. Radiation Model

In this section we derive equations for the components of the net radiation flux and their attenuation through the cloud layer. Net radiation flux is decomposed into net longwave and net shortwave components:

$$\mathrm{F}_{\mathrm{rad}}(z,t) = \mathrm{F}_{\mathrm{lw}}(z,t) - \mathrm{F}_{\mathrm{ls}}(z,t) \tag{11}$$

1) Liquid Water Path and Optical Depth

Both radiation terms are attenuated by an optical depth term designated as τ. This term depends on the total columnar liquid water content. We assume that the liquid water mixing ratio q_{l} within the cloud increases linearly with height proportional to a constant Γ_l, which can be calculated from thermodynamics or observations:

$$q_{\mathrm{l}}(z,t) = \begin{cases} \Gamma_l(z - z_{\mathrm{b}}(t)), & z_{\mathrm{b}}(t) \leq z \leq z_{\mathrm{i}}(t) \\ 0, & \text{otherwise} \end{cases} \tag{12}$$

The liquid water path (LWP) then becomes:

$$\mathrm{LWP}(z,t) = \int_{z'=z}^{z_{\mathrm{i}}(t)} \rho_{\mathrm{air}} q_{\mathrm{l}}(z',t)dz' = \begin{cases} 0, & z > z_{\mathrm{i}}(t) \\ \rho_{\mathrm{air}}\Gamma_l\left((z_{\mathrm{i}}(t) - z_{\mathrm{b}}(t))^2 - (z - z_{\mathrm{b}}(t))^2\right)/2, & z_{\mathrm{b}}(t) \leq z \leq z_{\mathrm{i}}(t) \\ \rho_{\mathrm{air}}\Gamma_l\left(z_{\mathrm{i}}(t) - z_{\mathrm{b}}(t)\right)^2/2, & z < z_{\mathrm{b}}(t) \end{cases} \tag{13}$$

The optical depth τ is defined with respect to the optical depth at the cloud top which is assumed to be zero. τ_{b} is the optical depth at and below the cloud base:

$$\tau(z,t) = \begin{cases} 0, & z > z_{\mathrm{i}}(t) \\ \dfrac{3\rho_{\mathrm{air}}\mathrm{LWP}}{2\mathrm{R_e}\rho_{\mathrm{W}}} = \dfrac{3\rho_{\mathrm{air}}\Gamma_l\left(h(t)^2 - (z - z_{\mathrm{b}}(t))^2\right)}{4\mathrm{R_e}\rho_{\mathrm{W}}}, & z_{\mathrm{b}}(t) \leq z \leq z_{\mathrm{i}}(t) \\ \tau_{\mathrm{b}}(t) \triangleq \dfrac{3\rho_{\mathrm{air}}\Gamma_l h^2}{4\mathrm{R_e}\rho_{\mathrm{W}}}, & z < z_{\mathrm{b}}(t) \end{cases} \tag{14}$$

ρ_{W} is the density of water and $\mathrm{R_e}$ is the effective droplet radius.

2) Longwave Radiation

For the longwave radiation, we utilize the model in Larson et al. (2007) which assumes isothermal blackbody radiation and single scattering. The net radiative longwave flux is defined as:

$$\mathrm{F_{lw}}(z,t) = \mathrm{L_{lw}}(t)e^{\alpha_{\mathrm{lw}}\tau(z,t)} + \mathrm{M_{lw}}(t)e^{-\alpha_{\mathrm{lw}}\tau(z,t)} \tag{15}$$

α_{lw} represents the optical depth scale for longwave radiation. The coefficients L and M are obtained by solving the second order radiation differential equation in Goody (1995):

$$\mathrm{L}_{\text{lw}}(t) = \gamma(t)\left((\mathrm{B}_{\text{cld}}(t)-\mathrm{B}_{\text{sky}}(t))\mathrm{c}_{1,\,\text{lw}}e^{-\alpha_{\text{lw}}\tau_{\text{b}}(t)}+(\mathrm{B}_{\text{srf}}(t)-\mathrm{B}_{\text{cld}}(t))\mathrm{c}_{2,\,\text{lw}}\right) \tag{16}$$

$$\mathrm{M}_{\text{lw}}(t) = \gamma(t)\left((\mathrm{B}_{\text{cld}}(t)-\mathrm{B}_{\text{sky}}(t))\mathrm{c}_{2,\,\text{lw}}e^{\alpha_{\text{lw}}\tau_{\text{b}}(t)}+(\mathrm{B}_{\text{srf}}(t)-\mathrm{B}_{\text{cld}}(t))\mathrm{c}_{1,\,\text{lw}}\right) \tag{17}$$

The coefficients are defined as:

$$\gamma(t) = \frac{-4\pi(1-\omega_{\text{lw}})}{\mathrm{c}_{1,\,\text{lw}}^2e^{-\alpha_{\text{lw}}\tau_{\text{b}}(t)}-\mathrm{c}_{2,\,\text{lw}}^2e^{\alpha_{\text{lw}}\tau_{\text{b}}(t)}} \tag{18}$$

$$\mathrm{c}_{1,\,\text{lw}} = \alpha_{\text{lw}}-2(1-\omega_{\text{lw}}) \tag{19}$$

$$\mathrm{c}_{2,\,\text{lw}} = \alpha_{\text{lw}}+2(1-\omega_{\text{lw}}) \tag{20}$$

$$\alpha_{\text{lw}} = \sqrt{3(1-\omega_{\text{lw}})(1-\omega_{\text{lw}}\mathrm{g}_{\text{lw}})} \tag{21}$$

ω_{lw} designates the single scattering albedo and g_{lw} is the asymmetry factor. The $\mathrm{B}_{\text{cld}}, \mathrm{B}_{\text{sky}}$ and B_{srf} terms are blackbody radiation arising from T_{cld}, T_{sky} and T_{srf}.

$$\mathrm{B}_{\text{cld}}(t)=\frac{\sigma}{\pi}\mathrm{T}_{\text{cld}}(t)^4, \qquad \mathrm{B}_{\text{sky}}(t)=\frac{\sigma}{\pi}\mathrm{T}_{\text{sky}}(t)^4, \qquad \mathrm{B}_{\text{srf}}(t)=\frac{\sigma}{\pi}\mathrm{T}_{\text{srf}}(t)^4 \tag{22}$$

T_{cld} and T_{srf} designate the effective radiation temperatures of the cloud base and ground surface, respectively. T_{sky} is the effective radiation temperature of the column above the cloud top.

3) Shortwave Radiation

We utilize the Delta-Eddington approximation in Duynkerke et al. (2004) and Shettle and Weinman (1970) as shortwave radiation model. Using the Eddington approximation, the diffuse radiance can be divided into a linear combination of a term independent of the solar zenith angle (θ_0) and a solar zenith angle dependent term, yielding the analytic solution for the net shortwave radiation flux as:

$$\mathrm{F}_{\text{ls}}(z,t)=F_0\mu_0(t)\left(\frac{4p}{3}\mathrm{L}_{\text{sw}}(t)e^{k\tau(z,t)}+\frac{4p}{3}\mathrm{M}_{\text{sw}}(t)e^{-k\tau(z,t)}+e^{-\tau(z,t)/\mu_0(t)}(1-\frac{4}{3}\beta_{sw}(t))\right) \tag{23}$$

$\omega_{\rm sw}$ designates the single scattering albedo for shortwave radiation, $\mathrm{g}_{\rm sw}$ is the asymmetry factor, $\mu_0 = \cos(\theta_0)$, A is the surface albedo and k is the optical depth scale for shortwave radiation. Note that the incoming downward shortwave radiation F_0 is different from the net shortwave radiation at the cloud top ($F_{ls}(z_i,t)$) as the net radiation includes radiation reflected from clouds and/or the ground surface. The coefficients are:

$$\beta_{\rm sw}(t) = 3\omega_{\rm sw}\frac{1+3\mathrm{g}_{\rm sw}(1-\omega_{\rm sw})\mu_0(t)^2}{4(1-k^2\mu_0(t)^2)} \tag{24}$$

$$\begin{aligned}\mathrm{L}_{\rm sw}(t) &= \frac{e^{-k\tau_{\rm b}(t)}\,(\alpha_{\rm sw}+2\beta_{\rm sw}/3)\,\mathrm{m}_1}{e^{k\tau_{\rm b}(t)}\mathrm{m}_2(1+2p/3)-e^{-k\tau_{\rm b}(t)}\mathrm{m}_1(1-2p/3)}\\ &- \frac{(1+2p/3)e^{-\tau_{\rm b}(t)/\mu_0(t)}\,(A(\alpha_{\rm sw}+2\beta_{\rm sw}/3-1)-(\alpha_{\rm sw}-2\beta_{\rm sw}/3))}{e^{k\tau_{\rm b}(t)}\mathrm{m}_2(1+2p/3)-e^{-k\tau_{\rm b}(t)}\mathrm{m}_1(1-2p/3)}\end{aligned} \tag{25}$$

$$\begin{aligned}\mathrm{M}_{\rm sw}(t) &= \frac{e^{k\tau_{\rm b}(t)}\,(\alpha_{\rm sw}+2\beta_{\rm sw}/3)\,\mathrm{m}_2}{e^{k\tau_{\rm b}(t)}\mathrm{m}_2(1+2p/3)-e^{-k\tau_{\rm b}(t)}\mathrm{m}_1(1-2p/3)}\\ &- \frac{(1-2p/3)e^{-\tau_{\rm b}(t)/\mu_0(t)}\,(A(\alpha_{\rm sw}+2\beta_{\rm sw}/3-1)-(\alpha_{\rm sw}-2\beta_{\rm sw}/3))}{e^{k\tau_{\rm b}(t)}\mathrm{m}_2(1+2p/3)-e^{-k\tau_{\rm b}(t)}\mathrm{m}_1(1-2p/3)}\end{aligned} \tag{26}$$

$$\mathrm{m}_1 = A(1+2p/3)-(1-2p/3), \qquad \mathrm{m}_2 = A(1-2p/3)-(1+2p/3) \tag{27}$$

$$k = \sqrt{3(1-\omega_{\rm sw})(1-\omega_{\rm sw}\mathrm{g}_{\rm sw})}, \qquad p = \sqrt{\frac{3(1-\omega_{\rm sw})}{1-\omega_{\rm sw}\mathrm{g}_{\rm sw}}} \tag{28}$$

$$\alpha_{\rm sw}(t) = 3\omega_{\rm sw}\mu_0(t)\frac{1+\mathrm{g}_{\rm sw}(1-\omega_{\rm sw})}{4(1-k^2\mu_0(t)^2)} \tag{29}$$

c. Boundary Conditions

To close the system of budget equations the boundary conditions at the ground surface and inversion are needed. Entrainment at the top can be expressed as a function of the virtual potential temperature flux, $\overline{w'\theta_{\rm v}'}$, through a convective velocity scale w^* defined as in Turton and Nicholls (1987), Caldwell et al. (2005) and Bretherton et al. (1999):

$${w^*}^3 = \frac{2.5g}{\theta_{\rm v,\,0}}\int_{z=0}^{z=z_{\rm i}}\overline{w'\theta_{\rm v}'}(z,t)dz, \qquad w_{\rm e}(t) = w^*\frac{\mathrm{A_w}}{\mathrm{Ri}}, \qquad \mathrm{Ri} = \frac{gz_{\rm i}\Delta\theta_{\rm v,\,i}}{\theta_{\rm v,\,0}{w^*}^2} \tag{30}$$

A_w is a tuning parameter, $\theta_{v,\,0}$ is a reference virtual potential temperature and Ri is the Richardson number. Combining the velocity scale equations and the Richardson number, we obtain:

$$w_e(t) = \frac{2.5A_w}{z_i(t)\Delta\theta_{v,\,i}} \int_{z=0}^{z_i(t)} \overline{w'\theta_v'}(z,t)dz \tag{31}$$

Finally, we need the surface boundary conditions to close the system of equations. Surface fluxes of heat and water are connected to the net surface radiation through surface flux efficiency, α_{srf} and the Bowen Ratio, β as (Ghonima et al. (2016)):

$$\mathrm{SHF}(t) = \overline{\mathrm{w}'\theta_l'}(0,t)\mathrm{c_p}\rho_{air} = -\alpha_{srf}\left(\frac{\beta}{\beta+1}\right)\mathrm{F_{rad}}(0,t) \tag{32}$$

$$\mathrm{LHF}(t) = \overline{\mathrm{w}'q_T'}(0,t)\mathrm{L_v}\rho_{air} = -\alpha_{srf}\left(\frac{1}{\beta+1}\right)\mathrm{F_{rad}}(0,t) \tag{33}$$

$\alpha_{srf} = 0.88$ is applied in all simulations while Bowen Ratio is also constant for a particular simulation, but will vary from simulation to simulation to investigate effects of soil moisture content.

Interdependencies of atmospheric variables are abundant as illustrated in Figure 2 through a automatically generated dependency graph.

3. Analytic Closed-Form Solution

a. Inversion Height Tendency

The objective of this section is to obtain a closed form solution for Eq. (2). This requires the entrainment velocity in Eq. (31) which depends on the virtual potential temperature flux $\overline{w'\theta_v'}(z,t)$. The virtual potential temperature flux depends on the surface heat fluxes as (Bretherton and Wyant (1997)):

$$\overline{w'\theta_v'}(z,t) = c_{1,3}\overline{\mathrm{w}'\theta_l'}(z,t) + c_{2,4}\overline{\mathrm{w}'q_T'}(z,t) \tag{34}$$

From the surface to the cloud base height the coefficients $c_{1,3} = c_1$ and $c_{2,4} = c_2$ are used. For the cloud layer, spanning from the cloud base height to the inversion height, $c_{1,3} = c_3$ and $c_{2,4} = c_4$ (Bretherton and Wyant (1997)).

We start by scaling Eq. (9) and Eq. (10) by $c_{1,3}$ and $c_{2,4}$, respectively and summing them up:

$$c_{1,3}\frac{d\theta_\mathrm{l}}{dt} + c_{2,4}\frac{dq_\mathrm{T}}{dt} = \frac{\overline{w'\theta_\mathrm{v}'}(0,t) + c_3 w_\mathrm{e}(t)\Delta\theta_{\mathrm{l,\,i}} + c_4 w_\mathrm{e}(t)\Delta q_{\mathrm{T,\,i}}}{z_\mathrm{i}(t)} + \frac{c_1\mathrm{F_{rad}}(0,t) - c_3\mathrm{F_{rad}}(z_\mathrm{i},t)}{\rho_\mathrm{air}\mathrm{c_p}z_\mathrm{i}(t)} \quad (35)$$

The left hand side can also be expressed using Eq. (4):

$$\begin{aligned} c_{1,3}\frac{d\theta_\mathrm{l}}{dt} + c_{2,4}\frac{dq_\mathrm{T}}{dt} &= -c_{1,3}\frac{\partial}{\partial z}\left(\overline{\mathrm{w}'\theta_\mathrm{l}'}(z,t) + \frac{\mathrm{F_{rad}}(z,t)}{\mathrm{c_p}\rho_\mathrm{air}}\right) - c_{2,4}\frac{\partial\overline{\mathrm{w}'q_\mathrm{T}'}(z,t)}{\partial z} \\ &= -c_{1,3}\frac{\partial}{\partial z}\left(\frac{\mathrm{F_{rad}}(z,t)}{\mathrm{c_p}\rho_\mathrm{air}}\right) - \frac{\partial\overline{w'\theta_\mathrm{v}'}(z,t)}{\partial z} \end{aligned} \quad (36)$$

Eq. (35) and Eq. (36) are equal to each other. We use the fact that the left side of both Eq. (35) and Eq. (36) are independent of z due to the well mixed assumption, to take the integral of both equations from $z = 0$ to an arbitrary z. Leaving the virtual potential temperature flux on the left side of the equation, the expression becomes:

$$\begin{aligned} \overline{w'\theta_\mathrm{v}'}(z,t) &= c_1\frac{\mathrm{F_{rad}}(0,t)}{\mathrm{c_p}\rho_\mathrm{air}} - c_{1,3}\frac{\mathrm{F_{rad}}(z,t)}{\mathrm{c_p}\rho_\mathrm{air}} + \overline{w'\theta_\mathrm{v}'}(0,t) \\ &+ \frac{z}{z_\mathrm{i}(t)}\left(\frac{c_3\mathrm{F_{rad}}(z_\mathrm{i},t) - c_1\mathrm{F_{rad}}(0,t)}{\rho_\mathrm{air}\mathrm{c_p}} - \overline{w'\theta_\mathrm{v}'}(0,t) - w_\mathrm{e}(t)(c_3\Delta\theta_{\mathrm{l,\,i}} + c_4\Delta q_{\mathrm{T,\,i}})\right) \end{aligned} \quad (37)$$

Utilizing the same scaling operation as in Eq. (35) for the surface flux definitions from Eq. (33) and Eq. (32):

$$\begin{aligned} \frac{c_1}{\mathrm{c_p}\rho_\mathrm{air}}\mathrm{SHF} + \frac{c_2}{\mathrm{L_v}\rho_\mathrm{air}}\mathrm{LHF} &= c_1\overline{\mathrm{w}'\theta_\mathrm{l}'}(0,t) + c_2\overline{\mathrm{w}'q_\mathrm{T}'}(0,t) = \overline{w'\theta_\mathrm{v}'}(0,t) \\ &= -\frac{\mathrm{F_{rad}}(0,t)}{\beta+1}\left(\frac{\alpha_\mathrm{srf}\beta c_1}{\mathrm{c_p}\rho_\mathrm{air}} + \frac{c_2\alpha_\mathrm{srf}}{\rho_\mathrm{air}\mathrm{L_v}}\right) \end{aligned} \quad (38)$$

Substituting Eq. (38) into Eq. (37), we obtain:

$$\begin{aligned} \overline{w'\theta_\mathrm{v}'}(z,t) = \frac{\mathrm{F_{rad}}(0,t)}{\mathrm{c_p}\rho_\mathrm{air}}\left(c_1 - \frac{\alpha_\mathrm{srf}\beta c_1}{\beta+1} - \frac{c_2\alpha_\mathrm{srf}\mathrm{c_p}}{\mathrm{L_v}(\beta+1)}\right) - c_{1,3}\frac{\mathrm{F_{rad}}(z,t)}{\mathrm{c_p}\rho_\mathrm{air}} \quad (39) \\ + \frac{z}{z_\mathrm{i}(t)}\left(\frac{c_3\mathrm{F_{rad}}(z_\mathrm{i},t)}{\rho_\mathrm{air}\mathrm{c_p}} - \frac{\mathrm{F_{rad}}(0,t)}{\rho_\mathrm{air}\mathrm{c_p}}\left(c_1 - \frac{\alpha_\mathrm{srf}\beta c_1}{\beta+1} - \frac{c_2\alpha_\mathrm{srf}\mathrm{c_p}}{\mathrm{L_v}(\beta+1)}\right) - w_\mathrm{e}(t)(c_3\Delta\theta_{\mathrm{l,\,i}} + c_4\Delta q_{\mathrm{T,\,i}})\right) \end{aligned}$$

Next, we integrate $\overline{w'\theta_v'}(z,t)$ over the boundary layer depth to obtain the entrainment velocity w_e in Eq. (31):

$$\begin{aligned} w_e(t) &= \frac{2.5\mathrm{A_w}}{z_i\Delta\theta_{v,\,i}}\left[\int\limits_{z=0}^{z=z_i}\left(1-\frac{z}{z_i}\right)\mathrm{F_{rad}}(0,t)\left(\frac{c_1}{\mathrm{c_p}\rho_{air}}-\frac{\alpha_{srf}\beta c_1}{\mathrm{c_p}\rho_{air}(\beta+1)}-\frac{c_2\alpha_{srf}}{\rho_{air}\mathrm{L_v}(\beta+1)}\right)dz\right. \\ &\left. - \int\limits_{z=0}^{z=z_i}\frac{c_{1,3}}{\mathrm{c_p}\rho_{air}}\mathrm{F_{rad}}(z,t)dz+\int\limits_{z=0}^{z=z_i}\frac{z}{z_i}\left(\frac{c_3\mathrm{F_{rad}}(z_i,t)}{\mathrm{c_p}\rho_{air}}-w_e\left(c_3\Delta\theta_{l,\,i}+c_4\Delta q_{T,\,i}\right)\right)dz\right] \end{aligned} \tag{40}$$

Combining all w_e terms on the left side, we obtain:

$$\begin{aligned} w_e(t)\left(\frac{0.8\Delta\theta_{v,\,i}}{\mathrm{A_w}}+c_3\Delta\theta_{l,\,i}+c_4\Delta q_{T,\,i}\right) &= \mathrm{F_{rad}}(0,t)\left(\frac{c_1}{\mathrm{c_p}\rho_{air}}-\frac{\alpha_{srf}\beta c_1}{\mathrm{c_p}\rho_{air}(\beta+1)}-\frac{c_2\alpha_{srf}}{\rho_{air}\mathrm{L_v}(\beta+1)}\right) \\ &+ \frac{c_3}{\mathrm{c_p}\rho_{air}}\mathrm{F_{rad}}(z_i,t)-\frac{2}{z_i\mathrm{c_p}\rho_{air}}\int\limits_{z=0}^{z=z_i}c_{1,3}\mathrm{F_{rad}}(z,t)dz \end{aligned} \tag{41}$$

Substituting this result in Eq. (2) we obtain the inversion height tendency:

$$\frac{dz_i(t)}{dt}-Dz_i=\zeta_1\mathrm{F_{rad}}(0,t)+\zeta_2\mathrm{F_{rad}}(z_i,t)+\frac{\zeta_3}{z_i}\int\limits_{z=0}^{z=z_i}c_{1,3}\mathrm{F_{rad}}(z,t)dz \tag{42}$$

where ζ coefficients are employed to simplify the equation. This is a nonlinear differential equation. Each net radiation term depends on the cloud thickness through the optical depth term. Furthermore, the columnar integral of the net radiation is called a Dawson function and is not an analytic function. Thus, an analytic solution requires approximations as explained in Section 3c.

b. Cloud Thickness Tendency

In addition to the inversion height tendency the cloud thickness tendency requires the cloud base height tendency. The solution strategy is to manipulate Eq. (3) into simpler variables analogous to the derivation of the inversion height tendency. The total moisture and liquid potential temperature tendencies appear in Eq. (3), but their tendencies given in Eq. (9) and Eq. (10), depend on z_i^{-1}. Since inversion height is a complex expression itself, it would be difficult to solve the tendencies in their current form. To simplify the inversion height dependency, we multiply both differential equations by z_i and add $\theta_\mathrm{l}\frac{dz_\mathrm{i}}{dt}$ and $q_\mathrm{T}\frac{dz_\mathrm{i}}{dt}$, respectively, so that the resulting expressions are the derivatives of the product of the conserved variables with the inversion height:

$$\begin{aligned}\frac{d\left(\theta_\mathrm{l}(t)z_\mathrm{i}(t)\right)}{dt} &= \overline{\mathrm{w}'\theta_\mathrm{l}'}(0,t)+\frac{\mathrm{F_{rad}}(0,t)}{\rho_\mathrm{air}\mathrm{c_p}}+w_\mathrm{e}(t)\theta_\mathrm{l,\,inv}-w_\mathrm{e}(t)\theta_\mathrm{l}(t)-\frac{\mathrm{F_{rad}}(z_\mathrm{i}(t),t)}{\rho_\mathrm{air}\mathrm{c_p}}+\theta_\mathrm{l}(t)\frac{dz_\mathrm{i}}{dt}\\ \frac{d\left(q_\mathrm{T}(t)z_\mathrm{i}(t)\right)}{dt} &= \overline{\mathrm{w}'q_\mathrm{T}'}(0,t)+w_\mathrm{e}(t)q_\mathrm{T,\,inv}-w_\mathrm{e}(t)q_\mathrm{T}(t)+q_\mathrm{T}(t)\frac{dz_\mathrm{i}}{dt}\end{aligned}$$

This manipulation simplifies the right side of the differential equation by eliminating the inversion height term. Only its tendency remains. Using the inversion tendency (Eq. (2)) and the surface fluxes (Eq. (32), Eq. (33)) we obtain:

$$\frac{d\left(\theta_\mathrm{l}(t)z_\mathrm{i}(t)\right)}{dt}-D\left(\theta_\mathrm{l}(t)z_\mathrm{i}(t)\right)=\left(\frac{\beta+1-\alpha_\mathrm{srf}\beta}{\rho_\mathrm{air}\mathrm{c_p}(\beta+1)}\right)\mathrm{F_{rad}}(0,t)-\frac{\mathrm{F_{rad}}(z_\mathrm{i}(t),t)}{\rho_\mathrm{air}\mathrm{c_p}}+w_\mathrm{e}(t)\theta_\mathrm{l,\,inv} \tag{43}$$

$$\frac{d\left(q_\mathrm{T}(t)z_\mathrm{i}(t)\right)}{dt}-D\left(q_\mathrm{T}(t)z_\mathrm{i}(t)\right)=-\frac{\alpha_\mathrm{srf}}{\mathrm{L_v}\rho_\mathrm{air}(\beta+1)}\mathrm{F_{rad}}(0,t)+w_\mathrm{e}(t)q_\mathrm{T,\,inv} \tag{44}$$

Note that we again need the net radiation expressions as in the inversion height expression to solve these differential equations. Finally, we use the cloud thickness tendency in Ghonima et al. (2015) to obtain the cloud thickness:

$$\frac{dh}{dt}=\frac{dz_\mathrm{i}(t)}{dt}-\frac{\mathrm{R_d T_{base}}}{gq_\mathrm{T}(t)}\left(1-\frac{\mathrm{L_v R_d}}{\mathrm{c_p R_v T_{base}}}\right)^{-1}\frac{dq_\mathrm{T}(t)}{dt}-\frac{\mathrm{c_p}\Pi_b}{g}\left(1-\frac{\mathrm{c_p R_v T_{base}}}{\mathrm{R_d L_v}}\right)^{-1}\frac{d\theta_\mathrm{l}(t)}{dt} \tag{45}$$

c. Approximation of Net Radiation Flux Term

The net radiation flux appears in three forms: 1) surface $\mathrm{F_{rad}}(0,t)$, 2) inversion height $\mathrm{F_{rad}}(z_\mathrm{i}(t),t)$, and 3) columnar average $\frac{1}{z_\mathrm{i}(t)}\int_{z=0}^{z=z_\mathrm{i}(t)}\mathrm{F_{rad}}(z,t)dz$. We start with the approximations for the net longwave expressions at $z=0$ and z_i based on Eq. (15). Then we continue with the net shortwave expressions at $z=0$ and z_i. Finally, we approximate the columnar integral of net radiation as a linear combination of the net radiation at $z=0$ and z_i.

$$\mathrm{F_{lw}}(\mathrm{z}=0,t)=\mathrm{L_{lw}}(t)e^{\alpha_\mathrm{lw}\tau_\mathrm{b}(t)}+\mathrm{M_{lw}}(t)e^{-\alpha_\mathrm{lw}\tau_\mathrm{b}(t)} \tag{46}$$

$$\mathrm{F_{lw}}(\mathrm{z}=z_\mathrm{i},t)=\mathrm{L_{lw}}(t)+\mathrm{M_{lw}}(t) \tag{47}$$

We simplify these expressions by neglecting higher order (< -1) exponential optical depth terms ($\exp(-\alpha_{\rm lw}\tau_{\rm b})$) as follows:

$$\mathrm{F_{lw}}(\mathrm{z},t) \simeq \frac{4\pi(1-\omega_{\rm lw})(\mathrm{B_{srf}}-\mathrm{B_{cld}})}{c_2}+\frac{8\pi\alpha_{\rm lw}(1-\omega_{\rm lw})(\mathrm{B_{cld}}-\mathrm{B_{sky}})}{c_2^2}e^{-\alpha_{\rm lw}\tau_b} \quad (48)$$

$$\mathrm{F_{lw}}(z_{\rm i}(t),t) \simeq \frac{4\pi(1-\omega_{\rm lw})(\mathrm{B_{cld}}-\mathrm{B_{sky}})}{c_2}+\frac{8\pi\alpha_{\rm lw}(1-\omega_{\rm lw})(\mathrm{B_{srf}}-\mathrm{B_{cld}})}{c_2^2}e^{-\alpha_{\rm lw}\tau_b} \quad (49)$$

Even though this simplification is not required for the analytic solution, it simplifies the sensitivity analysis in Section 5 and the error is less than 1%. Specifics for the error estimation are provided in Appendix B.b

To permit integration of net shortwave radiation into the cloud tendency expressions, we need to simplify solar zenith angle dependent terms, since solar zenith angle changes with time in a sinusoidal shape and complex nonlinear dependencies on μ_0 such as in Eq. (29) or the third exponential in Eq. (23) are difficult to integrate. We use the following approximations for $\alpha_{\rm sw}$ and $\beta_{\rm sw}$ in Eq. (29) and Eq. (24), with less than 2% and 1% error, respectively (see Appendix B.c).

$$\alpha_{\rm sw} \simeq 3\mu_0\omega_{\rm sw}\frac{1+\mathrm{g_{sw}}(1-\omega_{\rm sw})}{4}, \qquad \beta_{\rm sw} \simeq 3\omega_{\rm sw}/4 \quad (50)$$

To approximate the net shortwave radiation at the inversion height, we use its mathematical bounds at: clear sky, $\tau = 0$, and infinite depth, $\tau \to \infty$.

$$\mathrm{F_{ls}}(z=z_{\rm i},\tau_b=0)=F_0\mu_0(1-A), \qquad \mathrm{F_{ls}}(z=z_{\rm i},\tau_b\to\infty)=F_0\mu_0(1-\frac{4\beta_{sw}}{3+2p})+F_0\mu_0\frac{4p\alpha_{sw}}{3+2p} \quad (51)$$

The following approximation assumes an exponential dependence of net shortwave radiation on optical depth between these limits. The error of approximation is less than 6% (see Appendix B.c):

$$\mathrm{F_{ls}}(z=z_{\rm i}) \simeq \mathrm{F_{ls}}(z=z_{\rm i},\tau_{\rm b}\to\infty)+(\mathrm{F_{ls}}(z=z_{\rm i},\tau_{\rm b}\to\infty)-\mathrm{F_{ls}}(z=z_{\rm i},\tau_{\rm b}=0))\,e^{-2k\tau_{\rm b}} \quad (52)$$

The net shortwave radiation at the surface is approximated in terms of the value at the inversion height scaled by a factor of attenuation depending on the optical depth, with an error of less than

7% (see Appendix B.c):

$$\mathrm{F}_{\mathrm{ls}}(z=0) \simeq \mathrm{F}_{\mathrm{ls}}(z=z_{\mathrm{i}})e^{-k\tau_{\mathrm{b}}} \tag{53}$$

The columnar integral of net (shortwave and longwave) radiation flux can be approximated by a linear combination of net radiation values at the surface and inversion height with an error of 6% (see Appendix B.d):

$$\frac{1}{z_{\mathrm{i}}}\int_{z=0}^{z_{\mathrm{i}}} \mathrm{F}_{\mathrm{rad}}(z,t)dz \simeq s_1\mathrm{F}_{\mathrm{rad}}(z=0)+s_2\mathrm{F}_{\mathrm{rad}}(z=z_{\mathrm{i}}), \qquad s_1=0.99, s_2=0.04 \tag{54}$$

d. Inversion Height Solution

Using the simplified, integrable approximations for the net radiation terms a closed-form solution for the inversion height in Eq. (42) can be obtained. The columnar integral expression in Eq. (54) is employed to write Eq. (42) as a combination of net radiation terms at the surface and inversion height.

$$\frac{dz_{\mathrm{i}}(t)}{dt} - Dz_{\mathrm{i}}(t) = \psi_1(t)\mathrm{F}_{\mathrm{rad}}(0,t)+\psi_2(t)\mathrm{F}_{\mathrm{rad}}(z_{\mathrm{i}},t) \tag{55}$$

$$\psi_1 \triangleq \frac{\frac{c_1}{\mathrm{c_p}\rho_{\mathrm{air}}} - \frac{\alpha_{\mathrm{srf}}\beta c_1}{\mathrm{c_p}\rho_{\mathrm{air}}(\beta+1)} - \frac{c_2\alpha_{\mathrm{srf}}}{\rho_{\mathrm{air}}\mathrm{L_v}(\beta+1)} - \frac{2s_1}{\mathrm{c_p}\rho_{\mathrm{air}}}}{\frac{0.8\Delta\theta_{\mathrm{v,\,i}}}{\mathrm{A_w}}+c_3\Delta\theta_{\mathrm{l,\,i}}+c_4\Delta q_{\mathrm{T,\,i}}}, \qquad \psi_2 \triangleq \frac{\frac{c_3-2s_2}{\mathrm{c_p}\rho_{\mathrm{air}}}}{\frac{0.8\Delta\theta_{\mathrm{v,\,i}}}{\mathrm{A_w}}+c_3\Delta\theta_{\mathrm{l,\,i}}+c_4\Delta q_{\mathrm{T,\,i}}} \tag{56}$$

The solution strategy is to find all time dependent variables inside the net radiation expressions and then solve the differential equation. For net longwave (Eq. (15)) the blackbody radiations are time dependent and for net shortwave (Eq. (52) and (53)) the solar zenith angle is time dependent. Furthermore, both radiation terms depend on the optical depth exponentially and optical depth depends on the square of the cloud thickness given in Eq. (14). We use two approximations, which are further discussed in the following paragraphs: 1) Surface, cloud base, and cloud top effective temperatures are constant over a 24 hour period. As a result the blackbody radiation terms are constants. 2) The change in cloud thickness h is negligible compared to the radiation length scales. This means that the effect of change in optical depth can be ignored *only* for radiation terms resulting in constant exponential optical depth terms. The actual cloud thickness solution, $h(t)$, is not a constant and the actual time-dependent expression is presented in Section 3e.

The first approximation can be supported as follows: 1) The model is only valid in overcast conditions. In overcast conditions, the daily range in surface temperature compared to the actual temperature is small, where the root mean square error (RMSE) of the constant temperature assumption is about 6%, 2) Surface and cloud base temperatures follow similar diurnal patterns decreasing the error of the difference of blackbody radiation differences in Eq. (16) and Eq. (17). The RMSE of a constant blackbody difference assumption is about 4%. 3) The change in surface and cloud base temperatures is largest near solar noon due to the peak in net shortwave irradiance at small solar zenith angle. However, at noon the net longwave radiation is only $\sim$ 10% of the net shortwave radiation and therefore the longwave balance does not contribute significantly to the overall net radiation. In conclusion, it is justifiable to approximate the differences in blackbody radiations as constant. To further reduce the error, rather than using the initial temperatures at midnight, the mean temperatures of the previous day are used.

For the second approximation, we need to investigate the exponential optical depth terms for net longwave ($\exp(\alpha_{\mathrm{lw}}\tau_{\mathrm{b}})$) and net shortwave ($\exp(k\tau_{\mathrm{b}})$) expressions separately. Using the optical depth expression in Eq. (14), the exponent of the shortwave radiation can be written in the form of: $(h(t)/h_{\mathrm{sw}})^2$, where $h_{\mathrm{sw}} \triangleq \sqrt{(4\mathrm{R_e}\rho_{\mathrm{W}})/(3\rho_{\mathrm{air}}\Gamma_l k)}$, and $h_{sw} \sim [250, 500]$ m for k taken from Shettle and Weinman (1970), $\mathrm{R_e}$ from Larson et al. (2007), and for Γ_l between $[0.5, 2] \times 10^{-6}$ m^{-1}. The cloud thickness has to change on the order of h_{sw} to cause a significant change in the value of the exponent. The same notation for longwave yields the exponent in the form of: $(h(t)/h_{\mathrm{lw}})^2$ with $h_{\mathrm{lw}} = \sqrt{(4\mathrm{R_e}\rho_{\mathrm{W}})/(3\rho_{\mathrm{air}}\Gamma_l \alpha_{\mathrm{lw}})}$. $h_{\mathrm{lw}} >> h_{\mathrm{sw}}$, resulting in an even smaller exponent value than the shortwave. For a cloud thickness of 250 m, the RMSE of keeping the exponential optical depth term constant with respect to a varying numerical optical depth solution is $\sim$ 7% as demonstrated in Appendix B.e. The appendix also provides comparisons of daily model runs for constant and variable optical thickness under different Bowen Ratios and Γ_l values. The constant optical thickness results follows the variable optical thickness results, but differences increase for greater Γ_l and smaller Bowen Ratios. Large Γ_l result in smaller h_{sw} scales, causing larger deviation from the constant optical thickness assumption, whereas smaller Bowen Ratios delay cloud dissipation resulting in the accumulation of errors over longer time horizons.

Using both approximations, the only time dependent terms are the solar zenith angle terms, $\mu_0(t)$ and $\mu_0^2(t)$, and the inversion height tendency equation simplifies into:

$$\frac{dz_{\mathrm{i}}(t)}{dt} - Dz_{\mathrm{i}}(t) = a_1 + a_2\mu_0(t) + a_3\mu_0^2(t). \tag{57}$$

The solution of differential equations of type $\frac{dy}{dx} - Dy = f(x)$ is:

$$y(x) = y(0)e^{Dx} + e^{Dx}\int_{x'=0}^{x} e^{-Dx'} f(x')dx' \tag{58}$$

Assuming that $u_1(t)$, $u_2(t)$ and $u_3(t)$ are the solutions of

$$\frac{du_1}{dt} - Du_1 = 1, \qquad \frac{du_2}{dt} - Du_2 = \mu_0, \qquad \frac{du_3}{dt} - Du_3 = \mu_0^2 \tag{59}$$

we can write the inversion height as:

$$z_{\mathrm{i}}(t) = z_{\mathrm{i}}(0)e^{Dt} + a_1u_1(t) + a_2u_2(t) + a_3u_3(t) \tag{60}$$

We use the solar zenith angle definition of $\mu_0 = \max(\mu_1 + \mu_2\cos(t\pi/H - \pi), 0)$, where $\mu_1 = \sin(\mathrm{lat})\sin(\mathrm{dec})$, $\mu_2 = \cos(\mathrm{lat})\cos(\mathrm{dec})$, lat is the local latitude, dec is the declination and H is 12 hours. We solve for the functions u_1, u_2 and u_3 using Eq. (58). The equations for a single day are given below. The general forms for multiple days are more complex and provided in Appendix C.

$$
\begin{aligned}
u_1(t) &= \frac{e^{Dt}-1}{D} && (61)\\
u_2(t) &= \mu_2 \frac{\pi H^{-1}\sin(t\pi/H-\pi) - D\cos(t\pi/H-\pi)}{D^2+\pi^2 H^{-2}} \\
&+ e^{Dt-Dt_1}\frac{\pi H^{-1}\left(\sqrt{\mu_2^2-\mu_1^2}\right)+\mu_1 D^{-1}\pi^2 H^{-2}}{D^2+\pi^2H^{-2}} - \mu_1 D^{-1} && (62)\\
u_3(t) &= 2\mu_1\mu_2 \frac{\pi H^{-1}\sin(t\pi/H-\pi) - D\cos(t\pi/H-\pi)}{D^2+\pi^2 H^{-2}} \\
&+ 2\mu_1 e^{Dt-Dt_1}\frac{\pi H^{-1}\sqrt{\mu_2^2-\mu_1^2}-\mu_1 D}{D^2+\pi^2H^{-2}} \\
&+ \frac{\mu_2^2}{2}\frac{2\pi H^{-1}\sin(2t\pi/H) - D\cos(2t\pi/H)}{D^2+4\pi^2H^{-2}} \\
&+ e^{Dt-Dt_1}\frac{\pi D(\mu_1^2-\mu_2^2/2) - 2\mu_1\pi H^{-1}\sqrt{\mu_2^2-\mu_1^2}}{D^2+4\pi^2H^{-2}} && (63)
\end{aligned}
$$

The unit of these functions is seconds due to the time-integration. Using these functions, the inversion height can be calculated for any t without numerical integrations that would be required in mixed-layer models. The functional forms as plotted in Figure 3 directly reveal the following. At night time, when $\mu_0 = 0$, u_2 and u_3 follow the same exponential trend as u_1 as in $\exp(Dt)$ with additional oscillatory terms, therefore u_2 and u_3 decrease during the night. u_1 also follows a negative exponential trend due to the negative sign of D. This means that the combined effect of all three functions causes the inversion height to change exponentially and the exponent is the subsidence divergence parameter, D. D is hard to determine and difficult to measure; it typically assumes values on the order of $-[10^{-6}, 10^{-5}]$ s^{-1}. During the day, u_2 and u_3 increase, dominate over u_1 and behave like a sigmoid function. The signs and magnitudes of the coefficients for the u functions also determine the trends for the cloud base height as will be shown in Section 5.

Since the initial condition $z_i(0)$ is scaled by $\exp(Dt)$, the analytic solution also shows that the e-folding time for the effect of the initial condition $z_i(0)$ on the inversion height to approach zero is $1/D \sim 3$ days. This means that the initial inversion height has a negligible effect on the solution in ~ 3 days. Furthermore, since all u functions have the same exponential trend of $\exp(Dt)$, $z_\mathrm{i}(t)$ converges within 5% of steady state in approximately $1/3D \sim 9$ days. Once $z_\mathrm{i}(t)$ reaches the steady state solution, the inversion height oscillates with sinusoids of periods 12 hours and 24 hours. However, in practice this finding is largely irrelevant as the synoptic meteorological conditions induce change over shorter time scales rendering the mixed layer model results not applicable.

e. Cloud Thickness Solution

In order to obtain the final cloud thickness expression, the cloud base height expression is subtracted from the inversion height expression. In Eq. (3) only q_T and θ_l tendencies vary in time as the other terms are either constant or assumed constant due to the assumption of constant effective radiative temperature. We integrate Eq. (3) to obtain:

$$z_\mathrm{b}(t) - z_\mathrm{b}(0) = \frac{\mathrm{R_d T_{base}}}{g}\left(1 - \frac{\mathrm{L_v R_d}}{\mathrm{c_p R_v T_{base}}}\right)^{-1} \ln\left(\frac{q_\mathrm{T}(t)}{q_\mathrm{T}(0)}\right) + \frac{\mathrm{c_p}\Pi_b}{g}\left(1 - \frac{\mathrm{c_p R_v T_{base}}}{\mathrm{R_d L_v}}\right)^{-1}\theta_\mathrm{l}(t) \quad (64)$$

Assuming the change in $q_\mathrm{T}(t)$ to be small compared to its initial value, we use $\ln(x+1) \simeq x$ to linearize the expression and denote the coefficients of the time-varying terms as δ_1 and δ_2:

$$z_\mathrm{b}(t) - z_\mathrm{b}(0) = \delta_1(q_\mathrm{T}(t) - q_\mathrm{T}(0)) + \delta_2(\theta_\mathrm{l}(t) - \theta_\mathrm{l}(0)) \quad (65)$$

$$\frac{dz_\mathrm{b}(t)}{dt} = \delta_1\frac{dq_\mathrm{T}(t)}{dt} + \delta_2\frac{d\theta_\mathrm{l}(t)}{dt} \quad (66)$$

In Eq. (43) and Eq. (44) the $z_\mathrm{i}q_\mathrm{T}$ and $z_\mathrm{i}\theta_\mathrm{l}$ differentials are of the same functional form as the inversion height tendency. Thus, we manipulate the cloud base height expressions to obtain the same format so that the total moisture and liquid potential temperature results can be substituted directly. To achieve this, we multiply Eq. (65) by dz_i/dt and Eq. (66) by z_i and sum them up to obtain:

$$\frac{d(z_i z_b)}{dt} = \delta_1 \frac{d(z_i q_T)}{dt} + \delta_2 \frac{d(z_i \theta_l)}{dt} + \frac{dz_i}{dt}(z_b(0) - \delta_1 q_T(0) - \delta_2 \theta_l(0)) \tag{67}$$

Scaling Eq. (65) by Dz_i and subtracting it from Eq. (67) yields:

$$\frac{dz_i z_b}{dt} - Dz_i z_b = \delta_1 \left(\frac{d(z_i q_T)}{dt} - Dz_i q_T \right) + \delta_2 \left(\frac{d(z_i \theta_l)}{dt} - Dz_i \theta_l \right) \tag{68}$$

$$+ \left(\frac{dz_i}{dt} - Dz_i \right) (z_b(0) - \delta_1 q_T(0) - \delta_2 \theta_l(0)) \tag{69}$$

The $z_i q_T$ and $z_i \theta_l$ differentials can be substituted from Eq. (43) and Eq. (44):

$$\frac{dz_i(z_b - z_{adj})}{dt} - Dz_i(z_b - z_{adj}) = \frac{\delta_2 (\beta + 1 - \alpha_{srf}\beta) \mathrm{L_v} - \delta_1 \alpha_{srf} \mathrm{c_p}}{\rho_{air} \mathrm{c_p} \mathrm{L_v} (\beta + 1)} \mathrm{F_{rad}}(0,t) - \frac{\delta_2 \mathrm{F_{rad}}(z_i(t),t)}{\rho_{air} \mathrm{c_p}} \tag{70}$$

where $z_{adj} \triangleq z_b(0) + \delta_1 \Delta\theta_{l,\,i} + \delta_2 \Delta q_{T,\,i}$. Aggregating all constant coefficients in ψ_3 and ψ_4 we obtain:

$$\frac{dz_i(z_b - z_{adj})}{dt} - Dz_i(z_b - z_{adj}) = \psi_3 \mathrm{F_{rad}}(0,t) + \psi_4 \mathrm{F_{rad}}(z_i(t),t) \tag{71}$$

$$\psi_3 \triangleq \frac{\delta_2(1 - \alpha_{srf})}{\rho_{air} \mathrm{c_p}} + \frac{\delta_2 \alpha_{srf} \mathrm{L_v} - \delta_1 \alpha_{srf} \mathrm{c_p}}{\rho_{air} \mathrm{c_p} \mathrm{L_v} (\beta + 1)}, \qquad \psi_4 \triangleq -\frac{\delta_2}{\rho_{air} \mathrm{c_p}} \tag{72}$$

Eq. (70) depends only on the radiation terms which already had been derived for the inversion height expression:

$$z_i(t)(z_b(t) - z_{adj}) = z_i(0)(z_b(0) - z_{adj})e^{Dt} + b_0 u_1(t) + b_1 u_2(t) + b_2 u_3(t) \tag{73}$$

where the constants are combined into b_1, b_2 and b_3 for convenience. Solving for the cloud base height, we obtain:

$$z_b(t) = \frac{b_1 u_1(t) + b_2 u_2(t) + b_3 u_3(t) + z_i(0)(z_b(0) - z_{adj})e^{Dt}}{a_1 u_1(t) + a_2 u_2(t) + a_3 u_3(t) + z_i(0)e^{Dt}} + z_{adj} \tag{74}$$

And finally, the cloud thickness is obtained from $h(t) = z_i(t) - z_b(t)$.

4. Validation against LES

We verify our solution against Large Eddy Simulation (LES) specifically the UCLA-LES (Stevens et al. (2005)) on a 100×100 grid with 193 vertical levels. The horizontal resolution is 25 m and the vertical resolution is 5 m resulting in a domain of 2.5 km $\times$ 2.5 km $\times$ 960 m. The LES land surface model is a constant Bowen Ratio model that converts the incoming net radiation into SHF and LHF according to Eqs. (32) and Eq. (33). Initial conditions are CGILS s12 from Zhang et al. (2012) and initial profiles of q_{T} and θ_{l} are shown in Figure 4. The initial inversion height is 677 m, the initial cloud thickness is 238 m and LWP is 72.4 g m^{-2}. LES is initialized at 03:00 LST. The results for the first hour of integrations are considered spin-up time and not shown. LES is run for 23 more hours with samples taken every 20 seconds and averaged over 10 minutes. LES inversion height, cloud base height, inversion jumps for total moisture and liquid potential temperature, total moisture at the surface, and the effective radiative temperatures at the surface ($\mathrm{T_{srf}}$) and the cloud base ($\mathrm{T_{cld}}$) at 04:00 LST serve as initial conditions for the analytic model. The effective cloud top temperature ($\mathrm{T_{sky}}$) is obtained from the LES longwave flux, the constant value of the exponential optical depth ($\exp(k\tau_{\mathrm{b}})$) is calculated from LES shortwave flux and the subsidence divergence (D) is extracted from LES using Eq. (2).

The validation consisted of two sets of sensitivity experiments: 1) Varying Bowen Ratio and 2) Varying $\Delta q_{\mathrm{T,\,i}}$ jump at the inversion. Bowen Ratio sensitivity results in Figure 5 show agreement in the inversion height and cloud thickness time series, and cloud dissipation time; the inversion height RMSE compared to LES is less than 1.5% and the cloud thickness RMSE is less than 9%.

At this time, the cloud base height can also be compared against the *lifting condensation level* (LCL) - the level, where the moisture in air is expected to saturate based on surface temperature and relative humidity (Bolton (1980)). The LCL results for $\beta = 0.1$ and $\beta = 0.2$ in Figure 5 agree with our cloud thickness formulation. The small difference is due to the approximate nature of the LCL formulation. We use the current formulation (Ghonima et al. (2015)) for the rest of this paper, since it is integrated with the simulated MLM profiles. In contrast, the

LCL formulation depends on near-surface temperature and relative humidity, which would require additional equations to obtain the closed-form results.

Both inversion height (Eq. (56)) and cloud base height (Eq. (73)) were shown to depend on the inversion jump, including the total moisture jump, $\Delta q_{\mathrm{T,\,i}}$. Furthermore, the inversion jump also affects entrainment and the turbulent fluxes through the boundary conditions (Eqs. (7), (8)). Even though multiple interdependent variables depend on $\Delta q_{\mathrm{T,\,i}}$, we are able to infer how $\Delta q_{\mathrm{T,\,i}}$ affects the cloud thickness through our analytic solution. A detailed sensitivity analysis is presented in Section 5, where the analytic solution suggests that the inversion height decreases and cloud thickness increases with smaller magnitude inversion jumps. For the validation, LES were run for Bowen Ratios of 0.3 and 1 and the q_{T} jump was varied by ∓ 0.5 g kg^{-1} (moister and drier air in the free troposphere), while keeping the boundary layer value at 9.43 g kg^{-1}. Figure 6 shows that the analytic solution closely follows LES results in both trend and dissipation times. The inversion height RMSE compared to LES is again less than 1.5% and the cloud thickness RMSE is less than 5%. The cloud dissipates only for $\beta = 1$ and the time of dissipation differs only by 5 minutes.

5. Sensitivity Analysis

a. Inversion Height Sensitivity

In section 3, we found that the inversion height tendency is a linear combination of 3 functions: u_1, u_2 and u_3. The common property of these functions is that they generally increase exponentially and the exponent is the subsidence divergence (D). The evolution of the inversion height in time then depends on the coefficients of these functions given in Eq. (57), where the coefficients were kept in their compact forms to emphasize the linear combination of the three functions. Now, we write out these coefficients and analyze their dependence on the initial and boundary conditions.

$$a_1 = \frac{4\pi(1-\omega_{\mathrm{lw}})}{\mathrm{c}_{2,\,\mathrm{lw}}^2}\left((\mathrm{c}_{2,\,\mathrm{lw}}\psi_1 + 2e_{\mathrm{lw}}\alpha_{\mathrm{lw}}\psi_2)(\mathrm{B}_{\mathrm{srf}} - \mathrm{B}_{\mathrm{cld}}) \right.$$
$$\left. + (\mathrm{c}_{2,\,\mathrm{lw}}\psi_2 + 2e_{\mathrm{lw}}\alpha_{\mathrm{lw}}\psi_1)(\mathrm{B}_{\mathrm{cld}} - \mathrm{B}_{\mathrm{sky}})\right) \tag{75}$$

$$a_2 = -(\psi_2 + e_1\psi_1)F_0\left(1 - \frac{4\beta_{\mathrm{sw}}}{3+2p} + e_2\left(\frac{4\beta_{\mathrm{sw}}}{3+2p} - A\right)\right) \tag{76}$$

$$a_3 = -(1-e_2)(\psi_2 + e_1\psi_1)F_0\left(\frac{3p\omega_{\mathrm{sw}}(1+\mathrm{g}_{\mathrm{sw}}(1-\omega_{\mathrm{sw}}))}{3+2p}\right) \tag{77}$$

$$\psi_1 \triangleq \frac{\frac{c_1 - \alpha_{\mathrm{srf}}c_1 - 2s_1}{\mathrm{c_p}\rho_{\mathrm{air}}} + \frac{\alpha_{\mathrm{srf}}(c_1\mathrm{L_v} - c_2\mathrm{c_p})}{\mathrm{c_p}\rho_{\mathrm{air}}\mathrm{L_v}(\beta+1)}}{\frac{0.8\Delta\theta_{\mathrm{v,\,i}}}{\mathrm{A_w}} + c_3\Delta\theta_{\mathrm{l,\,i}} + c_4\Delta q_{\mathrm{T,\,i}}}, \qquad \psi_2 \triangleq \frac{\frac{c_3 - 2s_2}{\mathrm{c_p}\rho_{\mathrm{air}}}}{\frac{0.8\Delta\theta_{\mathrm{v,\,i}}}{\mathrm{A_w}} + c_3\Delta\theta_{\mathrm{l,\,i}} + c_4\Delta q_{\mathrm{T,\,i}}} \tag{78}$$

where for convenience, we defined $e_m \triangleq \exp(-mk\tau_{\mathrm{b}})$ and $e_{\mathrm{lw}} \triangleq \exp(-\alpha_{\mathrm{lw}}\tau_{\mathrm{b}})$ and remember that the exponential optical depth value ($\exp(-k\tau_{\mathrm{b}})$) was assumed to be constant in Section 3d.

The turbulent flux coefficients in Eq. (34), $c_1 = 1, c_2 = 108$ K$, c_3 = 0.5, c_4 = 970$ K, and the convective surface efficiency of $\alpha_{\mathrm{srf}} = 0.9$ in Eq. (32) and Eq. (33) are obtained from Ghonima et al. (2016). $\mathrm{A_w} = 0.2$ in Eq. (30) is from Turton and Nicholls (1987). Constants related to longwave radiation are from Larson et al. (2007) and shortwave radiation from Duynkerke et al. (2004). The coefficients become:

$$a_1 \simeq \frac{(39.55\times10^{-12}\ \mathrm{m\ s^{-1}\ K^{-3}})}{\zeta_D}\left(\left(\frac{1}{\beta+1} - 2.29 + 0.52e_{\mathrm{lw}}\right)(\mathrm{T}_{\mathrm{srf}}^4 - \mathrm{T}_{\mathrm{cld}}^4)\right.$$
$$\left. + \left(\frac{e_{\mathrm{lw}}}{\beta+1} - 2.31e_{\mathrm{lw}} + 0.51\right)(\mathrm{T}_{\mathrm{cld}}^4 - \mathrm{T}_{\mathrm{sky}}^4)\right) \tag{79}$$

$$a_2 \simeq \frac{(0.23\ \mathrm{m\ s^{-1}\ K})(0.23+e_2)}{\zeta_D}\left(2.3e_1 - 0.52 - \frac{e_1}{\beta+1}\right), \qquad a_3 \simeq (1-e_2)\frac{a_2}{1.53} \tag{80}$$

$$\zeta_D \triangleq 4\Delta\theta_{\mathrm{v,\,i}} + 0.5\Delta\theta_{\mathrm{l,\,i}} + (970\ \mathrm{K})\Delta q_{\mathrm{T,\,i}} \tag{81}$$

where ζ_D aggregates the inversion jumps and has been defined for notational convenience. The unit of ζ_D is K, $[\psi_1] = [\psi_2] =$ W^{-1} s^{-1} m^3, and $[a_1] = [a_2] = [a_3] =$ m s^{-1}.

Furthermore, a_2 is a scalar multiple of a_3, so we can combine the $u_2(t)$ and $u_3(t)$ functions into a new function $u_4(t) = u_2(t) + u_3(t)\frac{1-e_2}{1.53}$. Combining the coefficients, the inversion height expression becomes:

$$z_i(t) = z_i(0)e^{Dt} + a_1 u_1(t) + a_2 u_4(t) \tag{82}$$

The functions u_1 and u_4 are always positive. Thus, their combined tendency in time depends on the sign and magnitude of their coefficients. ζ_D is the common denominator of all coefficients and its only negative term is the inversion jump in total moisture. However, given the strong temperature inversions for the stratocumulus-topped marine boundary layer, the total moisture jump would have to be unrealistically large to create a negative sign for ζ_D. For example, if $\Delta\theta_{\mathrm{v,\,i}} = \Delta\theta_{\mathrm{l,\,i}} = 10$ K, the jump in total moisture would have to be 33 g kg^{-1} to reverse the sign, but typical values of q_{T} in the boundary layer are only 10 g kg^{-1}. Thus let us assume that $\zeta_D > 0$ K.

For the optical depth exponentials, e_1 and e_{lw}, a thinner cloud ranging between $[0, 200]$ m thickness and a thicker cloud in the interval $[200, 400]$ m are analyzed. For the thinner cloud, the optical depth variables are calculated as: $e_1 = 0.9, e_{\mathrm{lw}} = 0.39$; and for the thicker cloud: $e_1 = 0.7, e_{\mathrm{lw}} = 0.03$. For the thin cloud case, a_2 is positive for all Bowen Ratios. For a_1, there is a balance between the cloud base-cloud top and surface-cloud base blackbody radiation differences, slightly weighted towards the latter. The effect of Bowen Ratio is small due to its coefficient being small relative to the rest of the terms. A low radiative temperature for the cloud base favors positive a_1, whereas high surface or effective cloud top temperatures favor negative a_1. Using the standard atmospheric lapse rate of -6.5 K km^{-1} and assuming that effective radiative temperature equals air temperature, a_1 is always negative for the thin cloud case. A negative a_1 means that the inversion height increases proportionally with the cloud top temperature and inversely proportional with the surface temperature. This sounds counter-intuitive at first, as a large cloud top temperature would lead to a higher upwelling longwave radiation and thus faster cooling. However, for a thin cloud with low optical depth, a large proportion of the downwelling longwave radiation from the cloud top reaches the surface and contributes to the sensible heat flux. This leads to a temperature increase in the boundary layer, increasing the turbulent fluxes and entrainment, which results in increased inversion height.

For the thick cloud case, a_2 is positive for all Bowen Ratios. The sign of a_1 depends on both the Bowen Ratio and the radiative temperature balance. However, only the sign of the cloud top temperature term ($\mathrm{T_{sky}}$) is negative for all Bowen Ratios, thus the inversion height is inversely proportional to cloud top temperature. The change in the direction of the effect for a thicker cloud emerges since the cloud top net longwave radiation is attenuated through the cloud's high optical thickness and only a negligible fraction reaches the surface.

To infer the combined effect of the oscillating terms in Eq. (82), we need the numerical values of u_1 and u_4. For $D = -3.75 \times 10^{-6}\ \mathrm{s}^{-1}$, Julian day of 196 and latitude 32.85° N, $u_4 \approx 8.2 u_1$ in magnitude on average. For typical effective radiative temperatures, it is physically impossible for the weighted summation $(a_1 u_1 + a_2 u_4)$ to be negative. For example, for thin clouds if $\mathrm{T_{cld}} = \mathrm{T_{sky}}$, $\mathrm{T_{srf}}$ would have to be more than 560 K to cause a negative trend. Increasing Bowen Ratio increases a_2. Since u_4 is the dominant term, the combined trend increases with Bowen Ratio. To show this, we fix $\mathrm{T_{srf}}$, $\mathrm{T_{cld}}$, ζ_D, D and vary the Bowen Ratio and $\mathrm{T_{sky}}$, as shown in Figure 7.

Before sunrise $u_4 = 0$ such that the results represent only u_1 and all lines for both thin and thick clouds show a downward slope since the negative term of a_1 is dominant. This comes from the fact that a_1 includes only net longwave radiation terms. During the night, the net longwave radiation causes the boundary layer to cool decreasing the inversion height. For the thin cloud case, throughout the day higher cloud top temperatures are associated with larger inversion height since the cloud's optical thickness is small enough to admit net longwave radiation to the surface, which is converted into sensible heat flux and warms up the boundary layer. For the thick case, we see exactly the opposite, where higher cloud top temperature lead to lower inversion heights. A large optical thickness attenuates the cloud top radiation before it reaches the land surface, which results in a cooler mixing layer and reduces surface turbulent fluxes.

Larger Bowen Ratio causes z_i to increase by a factor of $1/(\beta+1)$ as is illustrated by the spacing between the gray lines of constant Bowen Ratios for $T_{sky} = 280$ K. Decreased moisture content in the soil associated with larger Bowen Ratio increases the sensible heat flux and the warming increases the inversion height. Since the ratio of radiation flux converted into turbulent fluxes is fixed through α_{srf}, the rate of the increases in the sensible heat flux and inversion height slow with increasing Bowen Ratio as reflected in the closer line spacing. Finally, the trend of the inversion height is also affected inversely by ζ_D. A larger jump in potential temperature results in a smaller change in inversion height, whereas a larger jump in the magnitude of total water mixing ratio causes in contrast a greater change. This arises mainly from the fact that the turbulent fluxes are bounded by the negative of the inversion jumps at the inversion layer, as presented in Eqs. (7), (8).

b. Cloud Base Height Sensitivity

For the sensitivity analysis of the cloud base height from Eq. (74) it is enlightening to analyze $z_i(z_b - z_{adj})$ as – similar to z_i – its functional form is a linear combination of the three u functions in Eq. (73). The coefficients of u_1, u_2, and u_3 are:

$$\begin{aligned} b_1 = \frac{4\pi(1-\omega_{lw})}{c_{2,\,lw}^2}\big((c_{2,\,lw}\psi_3 + 2e_{lw}\alpha_{lw}\psi_4)(B_{srf} - B_{cld}) \\ + (c_{2,\,lw}\psi_4 + 2e_{lw}\alpha_{lw}\psi_3)(B_{cld} - B_{sky})\big) \end{aligned} \tag{83}$$

$$b_2 = -(\psi_4 + e_1\psi_3)F_0\left(1 - \frac{4\beta_{sw}}{3+2p} + e_2\left(\frac{4\beta_{sw}}{3+2p} - A\right)\right) \tag{84}$$

$$b_3 = -(1-e_2)(\psi_4 + e_1\psi_3)F_0\left(\frac{3p\omega_{sw}(1+g_{sw}(1-\omega_{sw}))\alpha_{sw}}{3+2p}\right) \tag{85}$$

with

$$\psi_3 \triangleq \frac{\delta_2(1-\alpha_{srf})}{\rho_{air}c_p} + \frac{\delta_2\alpha_{srf}L_v - \delta_1\alpha_{srf}c_p}{\rho_{air}c_pL_v(\beta+1)}, \qquad \psi_4 \triangleq -\frac{\delta_2}{\rho_{air}c_p} \tag{86}$$

δ_1 and δ_2 from Eq. (66) are calculated using $q_T(0) = 9\ \mathrm{g\ kg^{-1}}$ as $-211590\ \mathrm{m\ K^{-1}}$ and $125\ \mathrm{m\ K^{-1}}$, respectively. The coefficients become:

$$b_1 \simeq \left(9.2\times 10^{-9}\ \mathrm{m^2\ s^{-1}\ K^{-4}}\right)\left(\left(\frac{1}{\beta+1}+1.88-2.21e_{\mathrm{lw}}\right)\left(\mathrm{T_{srf}^4}-\mathrm{T_{cld}^4}\right) + \left(\frac{e_{\mathrm{lw}}}{\beta+1}+1.88e_{\mathrm{lw}}-2.22\right)\left(\mathrm{T_{cld}^4}-\mathrm{T_{sky}^4}\right)\right) \quad (87)$$

$$b_2 \simeq (11\ \mathrm{m^2\ s^{-1}})(0.235+e_2)\left(7.33-e_1-\frac{12.43e_1}{\beta+1}\right), \qquad b_3 = (1-e_2)b_2/1.53 \quad (88)$$

The units of ψ_3 and ψ_4 are $\mathrm{W^{-1}\ s^{-1}\ m^4}$, and $[b_1]=[b_2]=[b_3]=\ \mathrm{m^2\ s^{-1}}$. As for the inversion height (Eq. (82)), u_2 and u_3 are combined into u_4:

$$z_{\mathrm{i}}(z_{\mathrm{b}}-z_{\mathrm{adj}}) = z_{\mathrm{i}}(0)(z_{\mathrm{b}}(0)-z_{\mathrm{adj}})e^{Dt}+b_1u_1(t)+b_2u_4(t) \quad (89)$$

As in the inversion height analysis in Section 5a, we consider two cases of thin and thick clouds with $e_1 = 0.9$, $e_{\mathrm{lw}} = 0.39$ and $e_1 = 0.7$, $e_{\mathrm{lw}} = 0.03$, respectively.

As with the coefficient of inversion height a_1, for b_1 there is a balance between the surface-cloud base and cloud base-cloud top radiation differences. Using a lapse rate for a standard atmosphere b_1 is negative for any Bowen Ratio. The equation for b_2 is very similar to a_2, except that for Bowen Ratios $\beta \geq 0.74$ for the thin cloud case and $\beta \geq 0.31$ for the thick cloud case, b_2 changes sign and becomes positive. The combined trend depends on the u_1 and u_4 functions. Since $u_4 \approx 8.2u_1$ and b_2 is much greater than b_1, b_2 is the dominant term in the equality. Therefore the sign of $z_{\mathrm{i}}(z_{\mathrm{b}}-z_{\mathrm{adj}})$ changes with the sign of b_2 during daytime. To show this, similar to the inversion height analysis, the sensitivity of β and $\mathrm{T_{sky}}$ is shown in Figure 8. The results for the daytime reflect sign and magnitude variation in u_4 with Bowen Ratio. As expected, cloud base height starts to increase during daytime at a Bowen Ratio of 0.47 and the cloud base height increases with increasing Bowen Ratio. The sensitivity to cloud top temperature is small due to the dominance of u_4. $z_{\mathrm{i}}(z_{\mathrm{b}}-z_{\mathrm{adj}})$ is only an intermediate expression that allows understanding cloud base height trends, but it does not have a physical meaning; instead Eq. (74) is considered now:

$$z_{\mathrm{b}}(t) = z_{\mathrm{b}}(0) + \frac{(b_1 + a_1(\delta_1 \Delta q_{\mathrm{T,\,i}} + \delta_2 \Delta \theta_{\mathrm{l,\,i}}))u_1(t) + (b_2 + a_2(\delta_1 \Delta q_{\mathrm{T,\,i}} + \delta_2 \Delta \theta_{\mathrm{l,\,i}}))u_4(t)}{z_{\mathrm{i}}(0)e^{Dt} + a_1 u_1(t) + a_2 u_4(t)} \tag{90}$$

Using the values from the sensitivity analysis for $z_{\mathrm{i}}(z_{\mathrm{b}} - z_{\mathrm{adj}})$ and z_{i}, and neglecting the u_1 terms as u_4 is the dominant term during daytime:

$$z_{\mathrm{b}}(t) \simeq z_{\mathrm{b}}(0) + (4.34\ \mathrm{m}^2)(0.23 + e_2)\left(15.6 + 13e_1 - \frac{38.6e_1}{\beta + 1}\right)\frac{u_4(t)}{z_{\mathrm{i}}(0)e^{Dt}} \tag{91}$$

For the thin cloud case, cloud base height changes direction for $\beta \geq 0.27$, whereas for the thick cloud case, the direction change occurs for $\beta \geq 0.1$. The cloud base height for different Bowen Ratios is plotted in Figure 9. This result shows that the cloud base height trend changes direction depending on the Bowen Ratio. Only a single cloud top temperature is shown as the effect of u_1 is negligible. Increasing Bowen Ratio causes a decrease in the latent heat flux and an increase in the sensible heat flux. The resulting drying and heating of the boundary layer increases the cloud base height more than the inversion height. The cloud then dissipates faster with increasing Bowen Ratios. The effect of Bowen Ratio decreases with increasing cloud optical thickness, as more radiation is absorbed or reflected within the cloud resulting in smaller surface turbulent fluxes.

Furthermore, note that the cloud base height converges to a steady state:

$$z_{\mathrm{b}}(t \to \infty) \simeq z_{\mathrm{b}}(0) + \delta_1 \Delta \theta_{\mathrm{l,\,i}} + \delta_2 \Delta q_{\mathrm{T,\,i}} + \frac{b_2}{a_2} = z_{\mathrm{adj}} + \frac{b_2}{a_2} \tag{92}$$

As shown earlier in this section, a_2 is positive and b_2 changes from negative to positive with higher Bowen Ratios. Therefore, larger Bowen Ratios lead to larger steady state cloud base height.

c. Cloud Thickness Sensitivity

Using inversion height and cloud base height trends, we can directly infer the cloud thickness sensitivity. In this section we study the maximum initial cloud thickness that can be dissipated 1) before sunrise, 2) before sunset or whether the cloud dissipates within 24 hours at all.

1) Cloud Thickness Evolution

Fig. 10 shows the thickness evolution of a cloud with 200 m initial thickness (top) and the resulting surface shortwave radiative fluxes, especially important from the solar forecasting aspect (bottom). The expected dissipation times using Eq. (94) and Eq. (96), later presented in this section, are tabulated in Table 1 for the cases in Fig. 10. The initial conditions used for the cases are also shown in Fig. 4.

The dashed lines compare the effect of Bowen Ratio under normal subsidence for an initial inversion height of 1500 m. Under these conditions, Eq. (94) predicts that the cloud does not dissipate before sunrise, but Eq. (96) predicts that the cloud dissipates during the day if $\beta > 0.3$. As expected in the figure only $\beta = 0.2$ does not dissipate. The lines with markers compare the same Bowen Ratio scenarios for a lower initial inversion height of 500 m. Under these conditions, the cloud dissipates at about the same time as for the initial inversion height of 1500 m for $\beta = 0.6$ and $\beta = 5$. Finally, the thick solid lines compare the effect of a strong subsidence for different initial inversion heights. As expected stronger subsidence decreases cloud thickness. For strong subsidence (-1.875×10^{-5} s^{-1}), Eq. (94) predicts that for $z_\mathrm{i}(0) > 1050$ m, the cloud dissipates before sunrise and Eq. (96) predicts that $z_\mathrm{i}(0) = 500$ m and $\beta > 0.16$ dissipates during the day. The results validate the analytically derived conditions.

2) Dissipation Before Sunrise

The expression for dissipation at t_sunrise will be derived to determine the critical initial cloud thickness, h_crit. In order for the cloud to dissipate, the initial cloud thickness must be less than h_crit. Before sunrise, $u_4 = 0$ and a_1 is negligible compared to b_1 such that:

$$h(t) = z_\mathrm{i}(0)e^{Dt} - z_\mathrm{b}(0) - \frac{b_1(e^{Dt}-1)}{z_\mathrm{i}(0)De^{Dt}} = h(0)e^{Dt} - (1-e^{Dt})\left(z_\mathrm{b}(0) - \frac{b_1}{e^{Dt}Dz_\mathrm{i}(0)}\right) \tag{93}$$

Since cloud thickness either monotonically increases or decreases during the night, the critical cloud thickness would dissipate exactly at sunrise. We manipulate Eq. (93) to obtain the maximum allowable initial cloud thickness for the dissipation condition to be satisfied:

$$h_{\text{crit}} \leq \left(1 - e^{Dt_{\text{sunrise}}}\right)\left(z_{\text{i}}(0) - \frac{b_1}{e^{Dt} D z_{\text{i}}(0)}\right) \simeq -t_{\text{sunrise}}\left(z_{\text{i}}(0)D - \frac{b_1}{e^{Dt} z_{\text{i}}(0)}\right) \tag{94}$$

We infer the following points from this condition: 1) Deeper boundary layers can dissipate thicker clouds. This comes from the fact that the contribution of the initial inversion height ($z_{\text{i}}(0)$) decreases in time through subsidence (Eq. (82)), whereas the initial cloud base height ($z_{\text{b}}(0)$) is not multiplied by a subsidence term in Eq. (90). For example, if surface, cloud base, and cloud top radiative temperatures were the same such that the net longwave radiation and related coefficients (a_1, b_1) are zero, the inversion height would still decrease in time due to subsidence, whereas cloud base height would stay constant as shown in Eq. (90). Thus, a larger inversion height subsides faster, resulting in more dissipation. The physical mechanism behind this is a faster subsidence rate due to a high inversion height. A faster subsidence rate results in a faster decrease in the cloud thickness; 2) Stronger subsidence dissipates thicker clouds. This is expected due to the faster decrease in the inversion height. The physical process is the same as the previous item. As the subsidence divergence increases, the subsidence rate of the cloud top also increases, resulting in a thinner cloud; 3) The cloud base analysis showed that b_1 is proportional to the cloud top temperature. Thus, a higher cloud top temperature increases the maximum ”dissipatable” cloud thickness before sunrise. However, a 1 K increase in T_{sky} only leads to approximately a 7.5 m increase in h_{crit}, thus T_{sky} has a smaller effect compared to the initial inversion height. The maximum dissipatable cloud thickness before sunrise for various cloud top temperatures, subsidence values, and initial inversion heights is presented in Figure 11.

3) Dissipation After Sunrise

The second dissipation option materializes through a closing of the gap between inversion height and cloud base height during the day due to a faster increase in cloud base height. Previously, we observed that the dominant daytime term is u_4. Dropping the u_1 terms, the cloud thickness expression can be written as:

$$h(t) = z_{\mathrm{i}}(0)e^{Dt} + a_2u_4(t) - z_{\mathrm{b}}(0) - \frac{(b_2 + a_2(\delta_1\Delta q_{\mathrm{T,\,i}} + \delta_2\Delta\theta_{\mathrm{l,\,i}}))u_4(t)}{z_{\mathrm{i}}(0)e^{Dt} + a_2u_4(t)} \tag{95}$$

The maximum dissipatable or critical initial cloud thickness at sunset is obtained as:

$$h_{\mathrm{crit}} \leq z_{\mathrm{i}}(0)(1 - e^{Dt_{\mathrm{sunset}}}) - a_2u_4(t_{\mathrm{sunset}}) + \frac{(b_2 + a_2(\delta_1\Delta q_{\mathrm{T,\,i}} + \delta_2\Delta\theta_{\mathrm{l,\,i}}))u_4(t_{\mathrm{sunset}})}{z_{\mathrm{i}}(0)e^{Dt_{\mathrm{sunset}}} + a_2u_4(t_{\mathrm{sunset}})} \tag{96}$$

Using $\Delta q_{\mathrm{T,\,i}} = -5\ \mathrm{g\ kg}^{-1}, \Delta\theta_{\mathrm{l,\,i}} = 10\ \mathrm{K}, \Delta\theta_{\mathrm{v,\,i}} = 10\ \mathrm{K}$, the critical thickness is obtained as:

$$\begin{aligned} h_{\mathrm{crit}} &= 0.23z_{\mathrm{i}}(0) + \frac{(13.96\times10^6\ \mathrm{m}^2)(0.14+0.6e_2)\left(0.4+0.32e_1-\frac{e_1}{\beta+1}\right)}{1.31z_{\mathrm{i}}(0)+(10^3\ \mathrm{m})(0.14+0.6e_2)\left(2.3e_1-0.52-\frac{e_1}{\beta+1}\right)} \\ &- (586\ \mathrm{m})(0.14+0.6e_2)\left(2.3e_1-0.52-\frac{e_1}{\beta+1}\right) \end{aligned} \tag{97}$$

For the thin cloud case, the critical thickness expression becomes:

$$h_{\mathrm{crit}} = \frac{0.23\left(z_{\mathrm{i}}(0)+(500\ \mathrm{m})\left(1.74+\frac{1}{\beta+1}\right)\right)^2 + (5.61\times10^6\ \mathrm{m}^2)\left(0.72-\frac{1}{\beta+1}\right)}{z_{\mathrm{i}}(0)+(430\ \mathrm{m})\left(1.72-\frac{1}{\beta+1}\right)} \tag{98}$$

We infer the following points based on this condition: 1) The dominant term is the negative Bowen Ratio dependent term in the numerator of Eq. (98). h_{crit} increases with increasing Bowen Ratio. However, the dependence on Bowen Ratio weakens as $1/\beta$ consistent with Section 5a. When the Bowen Ratio increases the positive feedback on the inversion height is weaker compared to the positive feedback on the cloud base height and the combined effect is an increase in h_{crit}. Since the net radiation flux that is converted into turbulent fluxes is constant, the sensitivity to Bowen Ratio decreases for high Bowen Ratios. 2) The dominant term changes sign with Bowen

Ratio, making dissipation impossible for small Bowen Ratios and possible for larger Bowen Ratios. Therefore there is a region of the parameter space without dissipation before sunset. The Bowen Ratio threshold that causes dissipation before sunset, is inversely proportional to the initial inversion height. 3) Larger initial inversion heights enhance dissipation (first quadratic term). As explained in the previous section for dissipation before sunrise, the term that contains the initial inversion height decreases exponentially with subsidence, whereas the term with the initial cloud base height persists in time. 4) Larger potential temperature inversion jumps and smaller magnitudes of total moisture inversion jumps enable dissipation as they have been shown in Section 5a to limit inversion height growth (Eq. (96)). 5) Stronger subsidence enables dissipation, resulting directly from the decrease in inversion height. We plot the maximum cloud thickness that can be dissipated during the day for various Bowen Ratios, subsidence values, and initial inversion heights in Figure 12. Combining both night and day results, stronger subsidence, larger inversion height and higher Bowen Ratio enable dissipation and result in higher h_{crit} values.

d. Extrema Analysis

One of the advantages of an analytic solution is the ability to analyze derivatives for extrema determination. Extrema may be of interest, e.g. in solar forecasting where the thickest cloud conditions determine the maximum required amount of back-up generation. We performed extrema analysis on inversion height and cloud thickness to find out where their minima and maxima occur. To find the extrema points, we take the first and second derivative of the inversion height Eq. (82):

$$\frac{dz_{\mathrm{i}}(t)}{dt} = z_{\mathrm{i}}(0)De^{Dt} + a_1 e^{Dt} + a_2 u_4'(t) \tag{99}$$

$$\frac{d^2 z_{\mathrm{i}}(t)}{dt^2} = z_{\mathrm{i}}(0)D^2 e^{Dt} + a_1 De^{Dt} + a_2 u_4''(t) = a_2(u_4''(t) - Du_4'(t)) \tag{100}$$

The extrema points are obtained by solving the equation:

$$\frac{dz_{\mathrm{i}}(t)}{dt} = 0 \rightarrow \frac{z_{\mathrm{i}}(0)D}{a_2} + \frac{a_1}{a_2} = -\frac{u_4'(t)}{e^{Dt}} \tag{101}$$

The terms of the equality are plotted in Figure 13. The extrema are close to sunrise and sunset. A greater initial inversion height leads to extrema moving towards mid-day. Furthermore, since $a_1/a_2 \ll 1$, the effect of Bowen Ratio and longwave and shortwave radiation terms is small compared to the initial inversion height.

The second derivative determines whether these points are maxima or minima. We know that $a_2 > 0, D < 0$ and $u_4''(t) \gg Du_4'(t)$. So the sign is determined by the sign of the second derivative of u_4. The sign is positive until mid-day as the cosine of the solar zenith angle is increasing and it is negative after mid-day. This means that the first extremum after sunrise is a minimum and the second extrema before sunset is a maximum. This is an expected result as during night time longwave cooling decreases the inversion height. A minimum occurs when after sunrise net shortwave radiation counteracts longwave cooling and eventually becomes dominant to increase z_{i}. Similarly in the afternoon, net shortwave radiation results in an increase in inversion height until longwave cooling dominates closer to sunset.

We continue with the cloud thickness expression. The cloud base height was (Eq. (90)):

$$z_{\mathrm{b}}(t) = \frac{z_{\mathrm{i}}(t)z_{\mathrm{adj}} + b_1u_1(t) + b_2u_4(t) + z_{\mathrm{i}}(0)(z_{\mathrm{b}}(0) - z_{\mathrm{adj}})e^{Dt}}{z_{\mathrm{i}}(t)} \tag{102}$$

The cloud thickness is obtained by subtracting cloud base height in Eq. (102) from $z_{\mathrm{i}}(t)$:

$$h(t) = \frac{z_{\mathrm{i}}^2(t) - z_{\mathrm{i}}(t)z_{\mathrm{adj}} - b_1u_1(t) - b_2u_4(t) - z_{\mathrm{i}}(0)(z_{\mathrm{b}}(0) - z_{\mathrm{adj}})e^{Dt}}{z_{\mathrm{i}}(t)} = \frac{z_{\mathrm{i}}^2(t) + bz_{\mathrm{i}}(t) + c(t)}{z_{\mathrm{i}}(t)} \tag{103}$$

The derivatives are:

$$\frac{dh(t)}{dt} = \left(1 - \frac{c(t)}{z_{\mathrm{i}}^2}\right)\frac{dz_{\mathrm{i}}(t)}{dt} + \frac{dc(t)}{dt}\frac{1}{z_{\mathrm{i}}(t)} = 0 \tag{104}$$

$$\frac{d^2h(t)}{dt^2} = \frac{2c(t)}{z_{\mathrm{i}}(t)^3}\left(\frac{dz_{\mathrm{i}}(t)}{dt}\right)^2 + \left(1 - \frac{c(t)}{z_{\mathrm{i}}(t)^2}\right)\frac{d^2z_{\mathrm{i}}(t)}{dt^2} + \frac{d^2c(t)}{dt^2}\frac{1}{z_{\mathrm{i}}(t)} - 2\frac{dc(t)}{dt}\frac{1}{z_{\mathrm{i}}^2(t)}\frac{dz_{\mathrm{i}}(t)}{dt} \tag{105}$$

The cloud thickness derivative contains the inversion height derivative. We expand the inversion height expression from Eq. (82) for the first derivative as:

$$\begin{aligned}\frac{dz_{\mathrm{i}}}{dt}z_{\mathrm{i}}^2 &= (b_1u_1' + b_2u_2' + b_3u_3' + Dz_{\mathrm{i}}(0)(z_{\mathrm{b}}(0) - z_{\mathrm{adj}})e^{Dt})(a_1u_1 + a_2u_2 + a_3u_3 + z_{\mathrm{i}}(0)e^{Dt}) \\ &\quad -(b_1u_1 + b_2u_2 + b_3u_3 + z_{\mathrm{i}}(0)(z_{\mathrm{b}}(0) - z_{\mathrm{adj}})e^{Dt})(a_1u_1' + a_2u_2' + a_3u_3' + Dz_{\mathrm{i}}(0)e^{Dt}) \quad (106)\end{aligned}$$

Using the fact that $u_1' - Du_1 = 1$, $u_2' - Du_2 = \mu_0$ and $u_3' - Du_3 = \mu_0^2$, the expression becomes:

$$\frac{dz_{\mathrm{i}}}{dt} = \left.\frac{(a_1b_2 - a_2b_1)u_4(t) - z_{\mathrm{i}}(0)e^{Dt}\left((b_1 + b_2\mu_0(t)) + (a_1 + a_2\mu_0(t))(z_{\mathrm{adj}} - z_{\mathrm{b}}(0))\right)}{z_{\mathrm{i}}^2}\right|_{t=t_{\mathrm{ext}}} \quad (107)$$

Eq. (107) states that the cloud thickness extrema points exist when the derivative of the inversion height is equal to the right hand side (RHS) of the expression. We utilize the sensitivity results presented previously in this section for all coefficients to assess the extrema of cloud thickness. During night time for $\mu_0 = u_4 = 0$ the RHS is positive. Therefore, no extremum is present before sunrise as the derivative of the inversion height was shown to be negative.

During daytime for large Bowen Ratios that lead to the dissipation of the cloud before sunset, the RHS has a small negative value close to zero due to the quadratic term in the denominator, $b_2 > 0$ and $a_2 > 0$. This means that the extrema, if they exist, are close to the extrema of the inversion height - right after sunrise and right before sunset - since the inversion height extrema are when the inversion height derivative is zero. Inversion height is increasing during the day, except between sunrise and the inversion height minimum and between the inversion height maximum and sunset. The extremum for cloud thickness must occur during these two intervals when the inversion height decreases and the RHS is negative.

When smaller Bowen Ratios lead to persistence of the cloud, the RHS changes sign during the day from negative to positive. Since the initial sign of RHS is negative, the first extremum between sunrise and the minimum inversion height still exists, however the other extremum shifts to the interval between the minimum inversion height and maximum inversion height, where the inversion height derivative is positive and matches the sign of the RHS.

We check for cloud thickness minima and maxima conditions for the inversion height extrema points. The sign of the following expression determines the extrema condition:

$$\left(1-\frac{c(t)}{z_{\mathrm{i}}(t)^2}\right)\frac{d^2 z_{\mathrm{i}}(t)}{dt^2}+\frac{d^2 c(t)}{dt^2}\frac{1}{z_{\mathrm{i}}(t)}$$

The sign depends on the initial inversion height. The sign is the opposite of the second derivative of the inversion height for small initial inversion heights and the same for large initial inversion heights. Therefore for shallow boundary layers, the morning cloud thickness extremum is a maximum and occurs between sunrise and the minimum inversion height and the afternoon extremum is a minimum. For higher boundary layers, the morning cloud thickness extremum is a minimum and the afternoon extremum is a maximum. However, since larger inversion heights were shown to increase h_{crit} in Section 5c, the afternoon maximum may not be observed as the cloud may already have dissipated before the extremum depending on the Bowen Ratio. Two examples are shown in Figure 14, where $\beta = 0.2$ and the only difference is the initial inversion height. As expected, the minimum and maximum switch intervals between the two examples.

Combining this extrema result with the inversion height extrema, we have three scenarios for dissipation: 1) Cloud dissipation occurs before the minimum inversion height and then no cloud thickness maximum occurs as e.g. for the high subsidence and $z_{\mathrm{i}}(0) \geq 1000$ m cases in Figure 10. 2) For larger initial inversion height, dissipation occurs after sunrise. 3) For small initial inversion height, dissipation occurs after sunrise and before sunset with a maximum after sunrise depending on the Bowen Ratio. Since the extrema analysis can only give the extrema of the cloud thickness and not the values at those points, it is possible that the cloud may dissipate before the minimum.

6. Conclusions

We have provided an analytic closed-form solution to the cloud thickness evolution of stratocumulus clouds in a mixed layer model framework with a focus on application over coastal lands. This solution enabled sensitivity studies for inversion height, cloud base height and cloud thickness. While the parameter space was not explored exhaustively, for the typical base case chosen here, the following parameters influenced cloud thickness: Bowen Ratio, subsidence, and initial inversion height. Critical initial cloud thicknesses, that can be dissipated pre and post-sunrise were derived. Furthermore, we provided extrema analyses for inversion height and cloud thickness expressions to show when these variables reach their maximum and minimum values. Cloud dissipation can occur pre-sunrise, but this situation is unlikely in practice as such adverse conditions would likely have prevented cloud formation in the first place. If cloud does not dissipate pre-sunrise, then a morning maximum and afternoon minimum in cloud thickness is observed. For large initial inversion heights, this observation is reversed as a morning minimum for cloud thickness. If this minimum is associated with a cloud thickness of zero then the cloud deck breaks up during the day. If the minimum is associated with a cloud thickness greater than zero, then clouds are guaranteed to be maintained throughout the day.

The work in this paper will be used as the fundamental building block for future research on physical effect on cloud lifetime. In the present analysis that does not consider advection, clouds are sustained only for unrealistically small Bowen Ratios. Even though our solution provided a good match against LES results, the models and assumptions that were required to solve the equations, limit its application compared to the variable meteorological conditions in the real world. Examples include soil moisture change, precipitation, wind profiles, advection, and decoupling. Future work will include large scale advection effects to analyze more realistic scenarios over coastal lands. We plan to create a multi-column structure, where the columns are coupled through large scale advection. The addition of moisture and cooling from the ocean is expected to increase the sustenance of the clouds over the coast, creating more realistic dissipation times. Furthermore, our current model does not consider the decoupling process. Even though decoupling occurs less frequently than the well-mixed conditions, multi-layer clouds can form in deep boundary layers that can result in the vertical column deviating from well-mixed conditions. Decoupling can occur under stronger winds and, stronger temperature and moisture gradients. We plan to extend our current model to study multiple cloud layers in a single column to observe the effects of decoupling on cloud dissipation.

Acknowledgement

The authors would like to thank Dr. Mohamed Ghonima and Dr. Joel Norris for helpful discussion and comments for this work.

APPENDIX A

Nomenclature

α_{lw} Optical depth scale for longwave radiation

α_{srf} Surface turbulent efficiency

$\mathrm{A_w}$ Entrainment tuning parameter

$\mathrm{B_{cld}}$ Cloud blackbody radiation

β Bowen Ratio

$\mathrm{B_{srf}}$ Surface blackbody radiation

B_{sky} Cloud top blackbody radiation

c_p Specific heat constant

$\Delta q_{T,\,i}$ Total water vapor mixing ratio jump at the inversion

$\Delta\theta_{l,\,i}$ Liquid potential temperature jump at the inversion

$\Delta\theta_{v,\,i}$ Virtual potential temperature jump at the inversion

F_{lw} Net longwave radiation flux

F_{rad} Net radiation flux

F_{ls} Net shortwave radiation flux

g_{lw} Asymmetry factor for longwave radiation

g_{sw} Asymmetry factor for shortwave radiation

L_v Latent heat of evaporation

μ_0 Cosine of the solar zenith angle

ω_{lw} Single scattering albedo for longwave radiation

ω_{sw} Single scattering albedo for shortwave radiation

q_l Liquid water mixing ratio

q_T Total water vapor mixing ratio

$q_{T,\,adv}$ Horizontal advection of water vapor mixing ratio

$q_{T,\,inv}$ Total water vapor mixing ratio at the inversion

R_d Gas constant for dry air

R_e Effective droplet radius

ρ_{air} Density of air

ρ_W Density of water

Ri Richardson number

R_v Gas constant for moist air

τ_b Optical depth of the cloud

T_{base} Cloud base temperature

T_{cld} Effective cloud temperature

θ_l Liquid potential temperature

$\theta_{l,\,adv}$ Horizontal advection of liquid potential temperature

$\theta_{l,\,inv}$ Liquid potential temperature at the inversion

θ_v Virtual potential temperature

$\theta_{v,\,0}$ Virtual potential temperature reference

T_{srf} Surface temperature

T_{sky} Effective cloud top cooling temperature

$\mathbf{v}_H$ Horizontal wind speed

w_e Entrainment velocity

$\overline{\mathrm{w}' q'_T}$ Mean turbulent flux for total water vapor mixing ratio

w_s Subsidence velocity

$\overline{w'\theta_l'}$ Mean turbulent flux for liquid potential temperature

$\overline{w'\theta_v'}$ Mean turbulent flux for virtual potential temperature

z_b Cloud base height

z_i Inversion height

D Subsidence divergence

g Gravitational acceleration

t Time

APPENDIX B

Error Calculations

a. Error Calculation Methods and Metrics

We use the root mean square error (RMSE) definition as:

$$\mathrm{RMSE} \triangleq \sqrt{\frac{1}{\mathrm{N}} \sum_{i=1}^{\mathrm{N}} \left(\mathrm{x}_{\mathrm{model}}(i) - \mathrm{x}_{\mathrm{ref}}(i)\right)^2} \tag{B1}$$

$\mathrm{x}_{\mathrm{model}}(i)$ represents the i^{th} point generated by our model, whereas $\mathrm{x}_{\mathrm{ref}}(i)$ is the i^{th} point associated with a reference (usually the ground truth). The percentage error is defined by normalizing the RMSE by the mean reference value:

$$\%\mathrm{Error} = \frac{\mathrm{RMSE}}{\frac{1}{\mathrm{N}} \sum\limits_{i=1}^{\mathrm{N}} \mathrm{x}_{\mathrm{ref}}(i)} \tag{B2}$$

This percentage error model is only used for positive valued variables.

Throughout this section, errors are assessed by comparing the results of our approximations with their original forms. For longwave calculations, we use the parameters from Larson et al. (2007) and for shortwave calculations we use the parameters from Duynkerke (1999). The errors are calculated numerically over a range of parameter values and then averaged. For inversion height, the interval of $z_i \in [500\text{ m}, 1000\text{ m}]$ with 50 m resolution is used, whereas for the cloud thickness $h \in [50\text{ m}, 400\text{ m}]$ is used. Since optical thickness depends on Γ_l, we use the interval $\Gamma_l \in [0.1\times 10^{-6}\text{ m}^{-1}, 2\times 10^{-6}\text{ m}^{-1}]$ with a resolution of $10^{-7}]$ m^{-1}. Longwave radiation depends on the surface, cloud, and cloud top effective radiative temperatures. The standard atmosphere adiabatic lapse rate of -6.5 K m^{-1} allows calculating the cloud and cloud top temperatures from the surface temperature. We use the interval $\text{T}_{\text{srf}} \in [285\text{ K}, 295\text{ K}]$ with 1 K resolution. For solar zenith angle calculations, we use daytime with 100 s resolution.

b. Longwave Error Calculations for the approximations in Eqs. (46) *and* (47)

We set $\omega_{\text{lw}} = 0.694$ and $\text{g}_{\text{lw}} = 0.83$ for all longwave calculations. We performed more than 35 million experiments, where we calculated the percentage error of our approximation in Eq. (49) and (48) with respect to the original formulation in Eq. (47) and (46). The maximum RMSE observed is 0.53 and the maximum percentage error is 0.05%, while the mean percentage error is 0.03%. The maximum error is observed for Eq. (47), $z_i = 500$ m, $\Gamma_l = 2\times 10^{-6}\text{ m}^{-1}$ and $\text{T}_{\text{srf}} = 285$ K.

c. Shortwave Error Calculations for the approximations in Eqs. (53) *and* (52)

We set $\omega_{\text{sw}} = 0.993$ and $\text{g}_{\text{sw}} = 0.83$ for all shortwave calculations. We calculate α_{sw} and β_{sw} (Eq. 50) and compare against Eq. (29) and Eq. (24), respectively to obtain the error performance. We performed more than 32 million experiments. The resulting mean percentage error is 2%. The percentage error of our approximation at the inversion height in Eq. (52) is 6% and the maximum RMSE observed is 43 $\mathrm{W\ m^{-2}}$. The maximum error is observed for the $z_\mathrm{i} = 500$ m, $\Gamma_l = 10^{-6}\ \mathrm{m}^{-1}$ and $z_\mathrm{b} = 335$ m case. For the shortwave approximation at the surface in Eq. (53), the percentage error is 7% and the maximum RMSE is 44 $\mathrm{W\ m^{-2}}$. The maximum error is observed for the $z_\mathrm{i} = 500$ m, $\Gamma_l = 10^{-6}\ \mathrm{m}^{-1}$ and $z_\mathrm{b} = 325$ m case.

d. Net Radiation Error Calculations for the approximations in Eq. (54)

We use the same configurations as in the previous sections b, c. The mean percentage error of the columnar integral linear approximation in Eq. (54) is 6% and the RMSE is 41 $\mathrm{W\ m^{-2}}$.

e. Constant Assumption Validations

The first assumption states that the surface, cloud base and cloud top temperature variations are small compared to the actual temperature. Assuming a 30 K sinusoidal variation during the day from 265 K to 295 K and back to 265 K, the RMSE of assuming a fixed temperature is only 4.5 K corresponding to less than 2% error. The errors are amplified to 6% in the black body radiation calculation due to the fourth-order temperature dependence. The second assumption states that similar trends in temperature will decrease the effective error since the equations depend on the difference of the black body radiations. To verify this claim we create a second temperature timeseries at a height of 1 km. Under the standard atmosphere assumption, the lapse rate is $-6.5\ \mathrm{K\ km^{-1}}$] so the second temperature timeseries therefore varies sinusoidally from 256.5 K to 286.5 K instead. The error of the difference of black body radiation drops to 5%. The third assumption states that the net shortwave radiation is greater than the net longwave radiation in the cloud layer during the day. Using the assumptions in the previous example, the average ratio of net shortwave to net longwave during the day is 8.7.

The constant optical depth assumption with τ_b calculated once using the initial thickness and then set constant is validated against a model run with a variable (real) optical depth that is solved iteratively at every minute. Different optical depth variation were created through two scenarios with different Bowen Ratios of 0.2 and 1. Furthermore, since the optical depth depends on Γ_l, we analyzed two scenarios with $\Gamma_l = 10^{-7}$ m^{-1} (Figure B1 - top) and $\Gamma_l = 5 \times 10^{-7}$ m^{-1} (Figure B1 - bottom). The results in Figure B1 show that the iterative and constant solutions are close in all Bowen Ratio cases. In the case of $\Gamma_l = 5 \times 10^{-7}$ m^{-1}, the distance between the solutions increase relative to the $\Gamma_l = 10^{-7}$ m^{-1} case. The main reason is that the LWP and the cloud optical depth are 5 times higher, resulting in the optical thickness scale (h_{sw}) that is 5 times smaller. The difference is largest for $\beta = 0.2$, since the cloud does not dissipate within 24 hours and the error accumulates over a longer time.

APPENDIX C

Derivation of u_1, u_2, u_3 functions

We start the solution from $u_1(t)$:

$$u_1(t) = e^{Dt} \int_{t'=0}^{t} e^{-Dt'} dt' \tag{C1}$$

$$= \frac{e^{Dt} - 1}{D} \tag{C2}$$

We continue with $u_2(t)$. This function involves the solar zenith angle and can be written in a general form as: $\mu_0(t) = \max\left\{\mu_1 + \mu_2 \cos\left(\frac{t\pi}{H} - \pi\right), 0\right\}$. The solution is as follows:

$$u_2(t) = e^{Dt} \int_{t'=0}^{t} e^{-Dt'} \max\left\{\mu_1 + \mu_2 \cos\left(\frac{t'\pi}{H} - \pi\right), 0\right\} dt' \tag{C3}$$

Note that the expression in the maximum is a periodic expression. The non-zero region within a day spans from t_1, sunrise, to t_2, sunset. If t is greater than 1 day, then the solar zenith angle expression will be repeated. The general solution for a time t on following days is:

$$
\begin{aligned}
u_2(t) &= e^{Dt}\left(\int_{t_1}^{t_2} e^{-Dt'}\mu_0(t')dt' + \ldots + \int_{t_1+2(n-1)H}^{t_2+2(n-1)H} e^{-Dt'}\mu_0(t')dt' + \int_{t_1+2nH}^{t} e^{-Dt'}\mu_0(t')dt'\right) \\
&= e^{Dt}\sum_{j=0}^{n-1} e^{-2DHj}\int_{t_1}^{t_2} e^{-Dt'}\mu_0(t')dt' + e^{Dt-2DHn}\int_{t_1}^{t-2nH} e^{-Dt'}\mu_0(t')dt' \qquad \text{(C4)} \\
&= e^{Dt}\left(\frac{1-e^{-2DHn}}{1-e^{-2DH}}\right)\int_{t_1}^{t_2} e^{-Dt'}\mu_0(t')dt' + e^{Dt-2DHn}\int_{t_1}^{t-2nH} e^{-Dt'}\mu_0(t')dt' \qquad \text{(C5)}
\end{aligned}
$$

We start with the solution of the integral with a general bound:

$$
\begin{aligned}
\int_{t_1}^{x} e^{Dx-Dt'}\mu_0(t') &= \mu_1 e^{Dx}\int_{t_1}^{x} e^{-Dt'}dt' + \mu_2 e^{Dx}\int_{t_1}^{x} e^{-Dt'}\cos(t'\pi/H-\pi)dt' \qquad \text{(C6)} \\
&= \frac{\mu_1}{D}\left(e^{Dx-Dt_1}-1\right) + \mu_2 e^{Dx}\int_{t'=t_1}^{x} \frac{e^{it'\pi/H-i\pi-Dt'}+e^{-it'\pi/H+i\pi-Dt'}}{2}dt' \qquad \text{(C7)} \\
&= \frac{\mu_1}{D}\left(e^{Dx-Dt_1}-1\right) \\
&+ \mu_2 e^{Dx}\frac{e^{ix\pi/H-i\pi-Dx}-e^{it_1\pi/H-i\pi-Dt_1}}{2i\pi/H-2D} \\
&+ \mu_2 e^{Dx}\frac{e^{-ix\pi/H+i\pi-Dt}-e^{-it_1\pi/H+i\pi-Dt_1}}{-2i\pi/H-2D} \qquad \text{(C8)} \\
&= \mu_2\frac{\pi H^{-1}\sin(x\pi/H-\pi)-D\cos(x\pi/H-\pi)}{D^2+\pi^2H^{-2}} \\
&+ e^{Dx-Dt_1}\frac{\pi H^{-1}\left(\sqrt{\mu_2^2-\mu_1^2}\right)-\mu_1 D}{D^2+\pi^2H^{-2}} \\
&+ \mu_1 D^{-1}e^{Dx-Dt_1} - \mu_1 D^{-1} \qquad \text{(C9)} \\
&= \mu_2\frac{\pi H^{-1}\sin(x\pi/H-\pi)-D\cos(x\pi/H-\pi)}{D^2+\pi^2H^{-2}} \\
&+ e^{Dx-Dt_1}\frac{\pi H^{-1}\left(\sqrt{\mu_2^2-\mu_1^2}\right)+\mu_1 D^{-1}\pi^2H^{-2}}{D^2+\pi^2H^{-2}} - \mu_1 D^{-1} \qquad \text{(C10)}
\end{aligned}
$$

Using this result, we construct u_2:

$$\begin{aligned} u_2(t) &= e^{Dt-Dt_2}\left(\frac{1-e^{-2DHn}}{1-e^{-2DH}}\right)\frac{\pi H^{-1}\left(\sqrt{\mu_2^2-\mu_1^2}\right)-\mu_1 D^{-1}\pi^2 H^{-2}}{D^2+\pi^2 H^{-2}} \\ &+ e^{Dt-Dt_1}\left(\frac{1-e^{-2DHn}}{1-e^{-2DH}}\right)\frac{\pi H^{-1}\left(\sqrt{\mu_2^2-\mu_1^2}\right)+\mu_1 D^{-1}\pi^2 H^{-2}}{D^2+\pi^2 H^{-2}} \\ &+ \mu_2\frac{\pi H^{-1}\sin(t\pi/H-\pi)-D\cos(t\pi/H-\pi)}{D^2+\pi^2 H^{-2}} \\ &+ e^{Dt-2DHn-Dt_1}\frac{\pi H^{-1}\left(\sqrt{\mu_2^2-\mu_1^2}\right)+\mu_1 D^{-1}\pi^2 H^{-2}}{D^2+\pi^2 H^{-2}}-\mu_1 D^{-1} \end{aligned} \tag{C11}$$

The resulting equation has three components: a constant, an oscillatory component with a periodicity of 24 hours and an exponentially decreasing component, which has subsidence as its exponent. As in the previous component, this means that the exponential term will vanish after roughly 10 days.

We continue with $u_3(t)$. We now deal with the square of the solar zenith angle. Taking the square of the expression, we obtain a very similar expression as before:

$$\begin{aligned} \mu_0^2 &= \mu_1^2+2\mu_1\mu_2\cos(t\pi/H-\pi)+\mu_2^2\cos^2(t\pi/H-\pi) \\ &= \left(\mu_1^2+\mu_2^2/2\right)+\left(2\mu_1\mu_2\cos(t\pi/H-\pi)\right)+\left(\mu_2^2/2\right)\cos(2t\pi/H) \end{aligned} \tag{C12}$$

We again start with the solution of the integral with a general bound for μ_0^2:

$$
\begin{aligned}
&= \left(\mu_1^2+\mu_2^2/2\right)e^{Dx}\int_{t_1}^{x} e^{-Dt'}dt' + 2\mu_1\mu_2 e^{Dx}\int_{t_1}^{x} e^{-Dt'}\cos(t'\pi/H-\pi)dt' \\
&+ \left(\mu_2^2/2\right)e^{Dx}\int_{t_1}^{x} e^{-Dt'}\cos(2t'\pi/H)dt'
\end{aligned}
\tag{C13}
$$

$$
\begin{aligned}
&= \frac{\left(\mu_1^2-\mu_2^2/2\right)}{D}\left(e^{Dx-Dt_1}-1\right) + 2\mu_1\mu_2 e^{Dx}\int_{t'=t_1}^{x} \frac{e^{it'\pi/H-i\pi-Dt'}+e^{-it'\pi/H+i\pi-Dt'}}{2}dt' \\
&+ \left(\mu_2^2/2\right)e^{Dx}\int_{t'=t_1}^{x} \frac{e^{2it'\pi/H-Dt'}+e^{-2it'\pi/H-Dt'}}{2}dt'
\end{aligned}
\tag{C14}
$$

$$
\begin{aligned}
&= \frac{\left(\mu_1^2+\mu_2^2/2\right)}{D}\left(e^{Dx-Dt_1}-1\right) \\
&+ 2\mu_1\mu_2 e^{Dx}\frac{e^{ix\pi/H-i\pi-Dx}-e^{it_1\pi/H-i\pi-Dt_1}}{2i\pi/H-2D} \\
&+ 2\mu_1\mu_2 e^{Dx}\frac{e^{-ix\pi/H+i\pi-Dt}-e^{-it_1\pi/H+i\pi-Dt_1}}{-2i\pi/H-2D} \\
&+ \left(\mu_2^2/2\right)e^{Dx}\frac{e^{2ix\pi/H-Dx}-e^{2it_1\pi/H-Dt_1}}{4i\pi/H-2D} \\
&+ \left(\mu_2^2/2\right)e^{Dx}\frac{e^{-2ix\pi/H-Dt}-e^{-2it_1\pi/H-Dt_1}}{-4i\pi/H-2D}
\end{aligned}
\tag{C15}
$$

$$
\begin{aligned}
&= \frac{\left(\mu_1^2-\mu_2^2/2\right)}{D}\left(e^{Dx-Dt_1}-1\right) \\
&+ 2\mu_1\mu_2\frac{\pi H^{-1}\sin(x\pi/H-\pi)-D\cos(x\pi/H-\pi)}{D^2+\pi^2H^{-2}} \\
&+ 2\mu_1 e^{Dx-Dt_1}\frac{\pi H^{-1}\sqrt{\mu_2^2-\mu_1^2}-\mu_1 D}{D^2+\pi^2H^{-2}} \\
&+ \frac{\mu_2^2}{2}\frac{2\pi H^{-1}\sin(2x\pi/H)-D\cos(2x\pi/H)}{D^2+4\pi^2H^{-2}} \\
&+ e^{Dx-Dt_1}\frac{D(\mu_1^2-\mu_2^2/2)-2\mu_1\pi H^{-1}\sqrt{\mu_2^2-\mu_1^2}}{D^2+4\pi^2H^{-2}}
\end{aligned}
\tag{C16}
$$

Using the respective x values we obtain:

$$
\begin{aligned}
&2\mu_1\left(\frac{1-e^{-2DHn}}{1-e^{-2DH}}\right)\Bigg(e^{Dt-Dt_2}\frac{\pi H^{-1}\sqrt{\mu_2^2-\mu_1^2}-\mu_1\pi^2H^{-2}}{D^2+\pi^2H^{-2}}\\
&\qquad+e^{Dt-Dt_1}\frac{\pi H^{-1}\sqrt{\mu_2^2-\mu_1^2}+\mu_1\pi^2H^{-2}}{D^2+\pi^2H^{-2}}\Bigg)\\
&-\left(\frac{1-e^{-2DHn}}{1-e^{-2DH}}\right)\Bigg(e^{Dt-Dt_2}\frac{2\pi H^{-1}\mu_1\sqrt{\mu_2^2-\mu_1^2}+D(\mu_1^2-\mu_2^2)}{D^2+4\pi^2H^{-2}}\\
&\qquad-e^{Dt-Dt_1}\frac{D(\mu_1^2-\mu_2^2)-2\mu_1\pi H^{-1}\sqrt{\mu_2^2-\mu_1^2}}{D^2+4\pi^2H^{-2}}\Bigg)\\
&\qquad+\frac{\left(\mu_1^2-\mu_2^2/2\right)}{D}\left(e^{Dt-2DnH-Dt_1}-1\right)+\\
&2\mu_1\mu_2\frac{\pi H^{-1}\sin(t\pi/H-\pi)-D\cos(t\pi/H-\pi)}{D^2+\pi^2H^{-2}}\\
&+2\mu_1e^{Dt-2DnH-Dt_1}\frac{\pi H^{-1}\sqrt{\mu_2^2-\mu_1^2}-\mu_1D}{D^2+\pi^2H^{-2}}\\
&+\frac{\mu_2^2}{2}\frac{2\pi H^{-1}\sin(2t\pi/H)-D\cos(2t\pi/H)}{D^2+4\pi^2H^{-2}}\\
&+e^{Dt-2DnH-Dt_1}\frac{D(\mu_1^2-\mu_2^2/2)-2\mu_1\pi H^{-1}\sqrt{\mu_2^2-\mu_1^2}}{D^2+4\pi^2H^{-2}}
\end{aligned}
\tag{C17}
$$

This is similar to the previous result and results in 3 different components: a constant, oscillatory and exponential component with subsidence as its exponent.

References

Bolton, D., 1980: The computation of equivalent potential temperature. *Monthly Weather Review*, **108 (7)**, 1046–1053, doi:10.1175/1520-0493(1980)108⟨1046:TCOEPT⟩2.0.CO;2, URL http://dx.doi.org/10.1175/1520-0493(1980)108⟨1046:TCOEPT⟩2.0.CO;2, http://dx.doi.org/10.1175/1520-0493(1980)108⟨1046:TCOEPT⟩2.0.CO;2.

Bony, S., 2005: Marine boundary layer clouds at the heart of tropical cloud feedback uncertainties in climate models. *Geophys. Res. Lett.*, **32 (20)**, doi:10.1029/2005gl023851, URL http://dx.doi.org/10.1029/2005GL023851.

Bretherton, C. S., S. K. Krueger, M. C. Wyant, P. Bechtold, E. Van Meijgaard, B. Stevens, and J. Teixeira, 1999: A GCSS boundary-layer cloud model intercomparison study of the first astex lagrangian experiment. *Boundary-Layer Meteorology*, **93 (3)**, 341, doi:10.1023/A:1002005429969, URL http://dx.doi.org/10.1023/A:1002005429969.

Bretherton, C. S., and M. C. Wyant, 1997: Moisture transport, lower-tropospheric stability, and decoupling of cloud-topped boundary layers. *J. Atmos. Sci.*, **54 (1)**, 148–167, doi:10.1175/1520-0469(1997)054⟨0148:mtltsa⟩2.0.co;2, URL http://dx.doi.org/10.1175/1520-0469(1997)054⟨0148:MTLTSA⟩2.0.CO;2.

Caldwell, P., C. S. Bretherton, and R. Wood, 2005: Mixed-layer budget analysis of the diurnal cycle of entrainment in southeast pacific stratocumulus. *J. Atmos. Sci.*, **62 (10)**, 3775–3791, doi:10.1175/jas3561.1, URL http://dx.doi.org/10.1175/JAS3561.1.

Duynkerke, P. G., 1999: Turbulence, radiation and fog in dutch stable boundary layers. *Boundary-Layer Meteorology*, **90 (3)**, 447, doi:10.1023/A:1026441904734, URL http://dx.doi.org/10.1023/A:1026441904734.

Duynkerke, P. G., and Coauthors, 2004: Observations and numerical simulations of the diurnal cycle of the EUROCS stratocumulus case. *Quarterly Journal of the Royal Meteorological Society*, **130 (604)**, 3269–3296, doi:10.1256/qj.03.139, URL http://dx.doi.org/10.1256/qj.03.139.

Eastman, R., and S. G. Warren, 2014: Diurnal cycles of cumulus, cumulonimbus, stratus, stratocumulus, and fog from surface observations over land and ocean. *Journal of Climate*, **27 (6)**, 2386–

2404, doi:10.1175/JCLI-D-13-00352.1, URL http://dx.doi.org/10.1175/JCLI-D-13-00352.1, http://dx.doi.org/10.1175/JCLI-D-13-00352.1.

Fang, M., B. A. Albrecht, V. P. Ghate, and P. Kollias, 2014: Turbulence in continental stratocumulus, part i: External forcings and turbulence structures. *Boundary-Layer Meteorology*, **150 (3)**, 341–360, doi:10.1007/s10546-013-9873-3, URL http://dx.doi.org/10.1007/s10546-013-9873-3.

Ghonima, M. S., T. Heus, J. R. Norris, and J. Kleissl, 2016: Factors controlling stratocumulus cloud lifetime over coastal land. *J. Atmos. Sci.*, **73 (8)**, 2961–2983, doi:10.1175/jas-d-15-0228.1, URL http://dx.doi.org/10.1175/JAS-D-15-0228.1.

Ghonima, M. S., J. R. Norris, T. Heus, and J. Kleissl, 2015: Reconciling and validating the cloud thickness and liquid water path tendencies proposed by R. Wood and J. J. van der Dussen et al. *J. Atmos. Sci.*, **72 (5)**, 2033–2040, doi:10.1175/jas-d-14-0287.1, URL http://dx.doi.org/10.1175/JAS-D-14-0287.1.

Goody, R., 1995: *Principles of atmospheric physics and chemistry*. Oxford University Press, 324 pp.

Jamaly, M., J. L. Bosch, and J. Kleissl, 2013: Aggregate ramp rates of distributed photovoltaic systems in san diego county. *IEEE Transactions on Sustainable Energy*, **4 (2)**, 519–526, doi:10.1109/TSTE.2012.2201966.

Klein, S. A., and D. L. Hartmann, 1993: The seasonal cycle of low stratiform clouds. *Journal of Climate*, **6 (8)**, 1587–1606, doi:10.1175/1520-0442(1993)006⟨1587:TSCOLS⟩2.0.CO;2, URL http://dx.doi.org/10.1175/1520-0442(1993)006⟨1587:TSCOLS⟩2.0.CO;2, http://dx.doi.org/10.1175/1520-0442(1993)006⟨1587:TSCOLS⟩2.0.CO;2.

Kollias, P., and B. Albrecht, 2000: The turbulence structure in a continental stratocumulus cloud from millimeter-wavelength radar observations. *Journal of the Atmospheric Sciences*, **57 (15)**, 2417–2434, doi:10.1175/1520-0469(2000)057⟨2417:TTSIAC⟩2.0.CO;2, URL http://dx.doi.org/10.1175/1520-0469(2000)057⟨2417:TTSIAC⟩2.0.CO;2, http://dx.doi.org/10.1175/1520-0469(2000)057⟨2417:TTSIAC⟩2.0.CO;2.

Larson, V. E., K. E. Kotenberg, and N. B. Wood, 2007: An analytic longwave radiation formula for liquid layer clouds. *Monthly Weather Review*, **135 (2)**, 689–699, doi:10.1175/mwr3315.1, URL http://dx.doi.org/10.1175/MWR3315.1.

Lilly, D. K., 1968: Models of cloud-topped mixed layers under a strong inversion. *Quarterly Journal of the Royal Meteorological Society*, **94 (401)**, 292–309, doi:10.1002/qj.49709440106, URL http://dx.doi.org/10.1002/qj.49709440106.

Rémillard, J., P. Kollias, E. Luke, and R. Wood, 2012: Marine boundary layer cloud observations in the azores. *Journal of Climate*, **25 (21)**, 7381–7398, doi:10.1175/JCLI-D-11-00610.1, URL http://dx.doi.org/10.1175/JCLI-D-11-00610.1, http://dx.doi.org/10.1175/JCLI-D-11-00610.1.

Seager, R., M. B. Blumenthal, and Y. Kushnir, 1995: An advective atmospheric mixed layer model for ocean modeling purposes: Global simulation of surface heat fluxes. *Journal of Climate*, **8 (8)**, 1951–1964, doi:10.1175/1520-0442(1995)008⟨1951:AAAMLM⟩2.0.CO;2, URL http://dx.doi.org/10.1175/1520-0442(1995)008⟨1951:AAAMLM⟩2.0.CO;2, http://dx.doi.org/10.1175/1520-0442(1995)008⟨1951:AAAMLM⟩2.0.CO;2.

Serpetzoglou, E., B. A. Albrecht, P. Kollias, and C. W. Fairall, 2008: Boundary layer, cloud, and drizzle variability in the southeast pacific stratocumulus regime. *Journal of Climate*, **21 (23)**, 6191–6214, doi:10.1175/2008JCLI2186.1, URL http://dx.doi.org/10.1175/2008JCLI2186.1, http://dx.doi.org/10.1175/2008JCLI2186.1.

Shettle, E. P., and J. A. Weinman, 1970: The transfer of solar irradiance through inhomogeneous turbid atmospheres evaluated by Eddington's approximation. *J. Atmos. Sci.*, **27 (7)**, 1048–1055, doi:10.1175/1520-0469(1970)027⟨1048:ttosit⟩2.0.co;2, URL http://dx.doi.org/10.1175/1520-0469(1970)027⟨1048:TTOSIT⟩2.0.CO;2.

Stevens, B., 2002: Entrainment in stratocumulus-topped mixed layers. *Quarterly Journal of the Royal Meteorological Society*, **128 (586)**, 2663–2690, doi:10.1256/qj.01.202, URL http://dx.doi.org/10.1256/qj.01.202.

Stevens, B., and Coauthors, 2005: Evaluation of Large-Eddy Simulations via observations of nocturnal marine stratocumulus. *Mon. Wea. Rev.*, **133 (6)**, 1443–1462, doi:10.1175/mwr2930.1, URL http://dx.doi.org/10.1175/mwr2930.1.

Turton, J. D., and S. Nicholls, 1987: A study of the diurnal variation of stratocumulus using a multiple mixed layer model. *Quarterly Journal of the Royal Meteorological Society*, **113 (477)**, 969–1009, doi:10.1002/qj.49711347712, URL http://dx.doi.org/10.1002/qj.49711347712.

van der Dussen, J. J., S. R. de Roode, and A. P. Siebesma, 2014: Factors controlling rapid stratocumulus cloud thinning. *Journal of the Atmospheric Sciences*, **71 (2)**, 655–664, doi:10.1175/JAS-D-13-0114.1, URL http://dx.doi.org/10.1175/JAS-D-13-0114.1, http://dx.doi.org/10.1175/JAS-D-13-0114.1.

Zhang, M., C. S. Bretherton, P. N. Blossey, S. Bony, F. Brient, and J.-C. Golaz, 2012: The CGILS experimental design to investigate low cloud feedbacks in general circulation models by using single-column and Large-Eddy Simulation models. *Journal of Advances in Modeling Earth Systems*, **4 (4)**, doi:10.1029/2012MS000182, URL http://dx.doi.org/10.1029/2012MS000182, m12001.

LIST OF TABLES

TABLE 1. Projected critical cloud thickness values for the cases in Fig. 10.

	$\beta = 0.2, z_i(0) = 1500$ m, D_n	$\beta = 0.6, z_i(0) = 1500$ m, D_n	$\beta = 5, z_i(0) = 1500$ m, D_n
Before sunrise	75 m	56 m	13 m
Before sunset	19 m	506 m	1401 m
Dissipation Time	none	9.7 hours	7.9 hours
	$\beta = 0.2, z_i(0) = 500$ m, D_n	$\beta = 0.6, z_i(0) = 500$ m, D_n	$\beta = 5, z_i(0) = 500$ m, D_n
Before sunrise	0 m	0 m	0 m
Before sunset	0 m	500 m	500 m
Dissipation Time	none	9.2 hours	7.7 hours
	$\beta = 0.2, z_i(0) = 500$ m, $5D_n$	$\beta = 0.6, z_i(0) = 1000$ m, $5D_n$	$\beta = 5, z_i(0) = 1500$ m, $5D_n$
Before sunrise	26 m	190 m	330 m
Before sunset	211 m	1000 m	1500 m
Dissipation Time	16.7 hours	5.3 hours	2.8 hours

LIST OF FIGURES

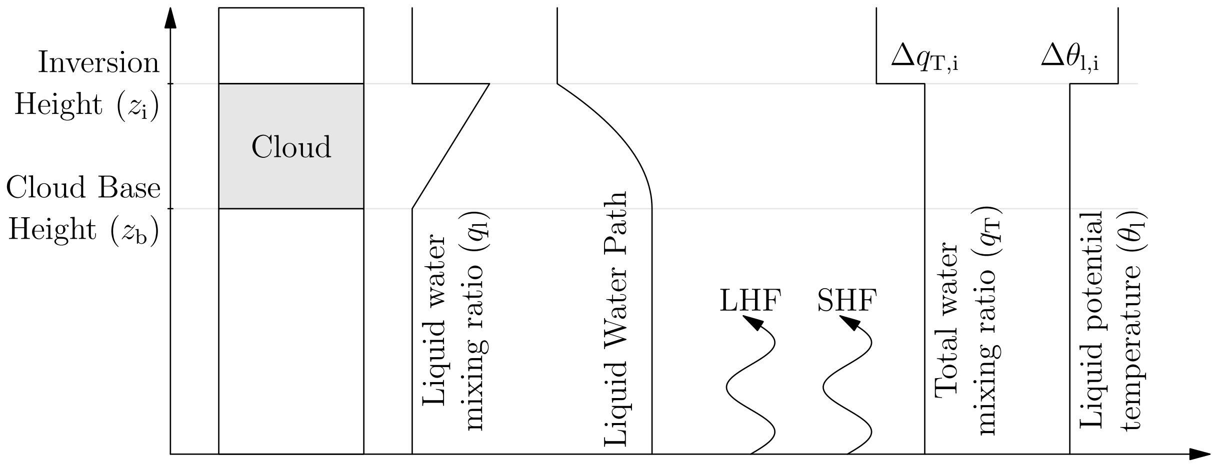

FIG. 1. Simulation domain. The system is modeled as a single well-mixed air column. The stratocumulus cloud layer (gray) is bounded by the temperature inversion and cloud base. The liquid water content q_{l} linearly increases with height in the cloud layer and the resulting liquid water path is shown. The surface boundary conditions of latent (LHF) and sensible heat fluxes (SHF) are also shown.

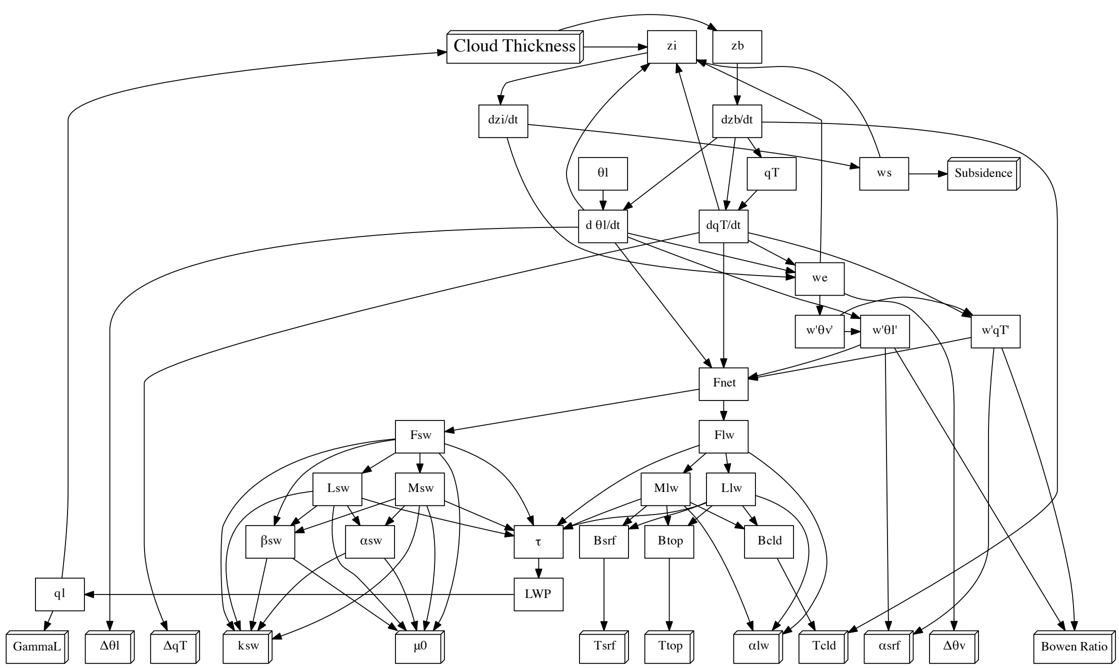

FIG. 2. Dependency graph for all variables in the system. An arrow between two variables indicates a dependency, where the source of the arrow *depends* on the end of it, e.g. Cloud thickness depends on inversion height.

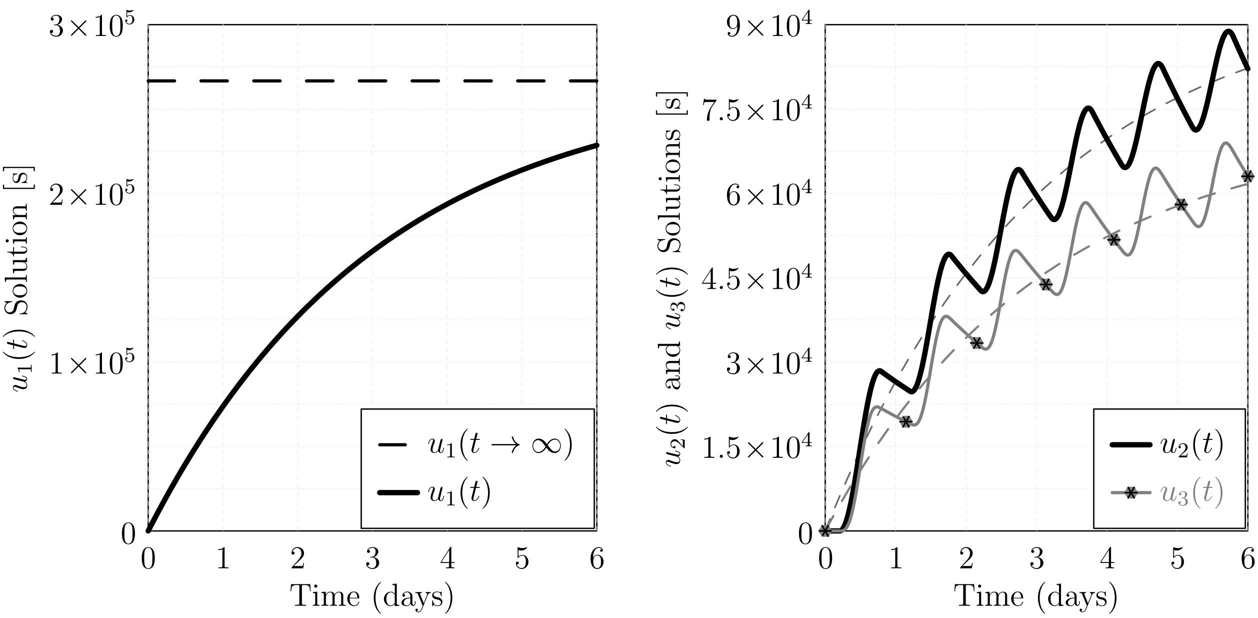

FIG. 3. Time evolutions of the $u_1(t)$, $u_2(t)$ and $u_3(t)$ functions that constitute the inversion height solution in Eq. (60). For subsidence, $D = -3.75\times10^{-6}$ s^{-1} is used. Solar zenith angle is calculated for a latitude of 32.85° N and the 196th day of the year.

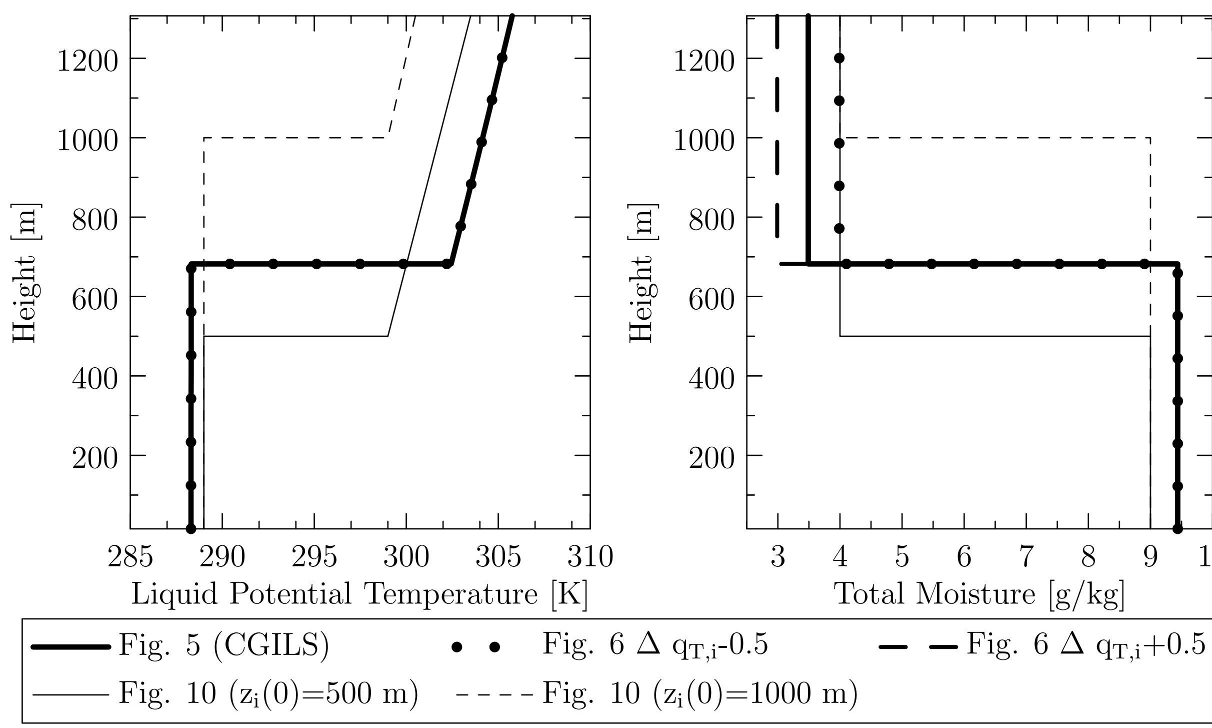

FIG. 4. Initial profiles of liquid potential temperature and total water mixing ratio used for LES are taken from CGILS s12 data (thick solid line). Throughout this work, the initial profiles have been slightly modified to study various conditions, such as total moisture jump sensitivity in Fig. 6 (dotted and thick dashed lines) and initial inversion height sensitivity in Fig. 10 (thin solid and dashed lines).

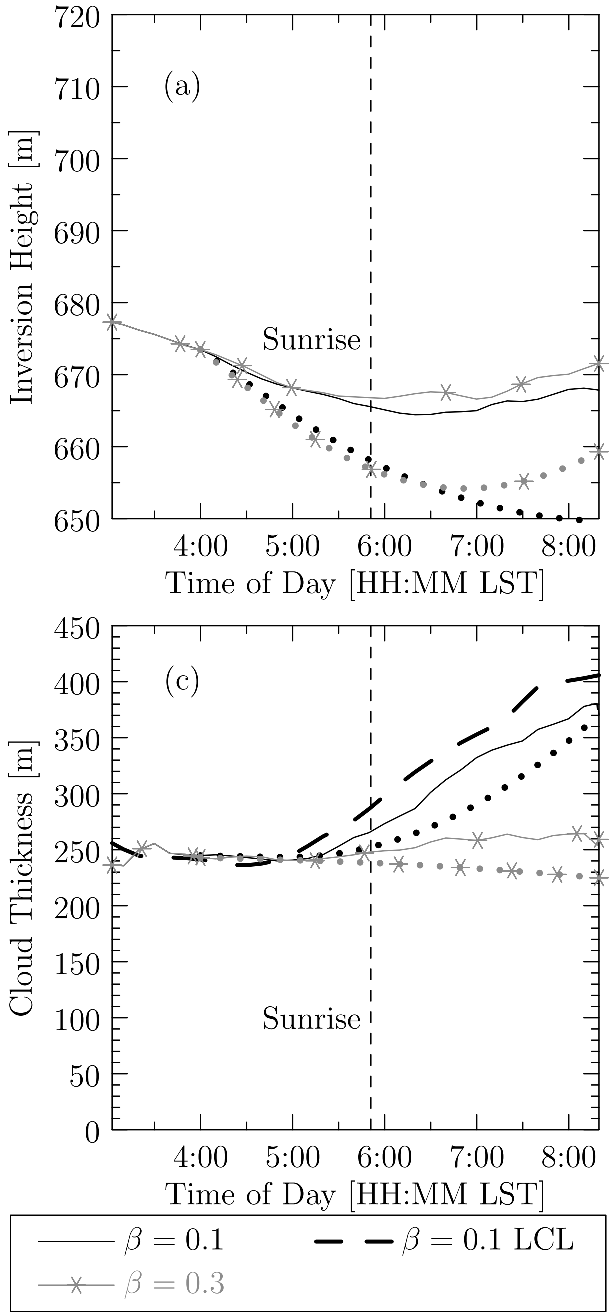

FIG. 5. Bowen Ratio sensitivity comparison between the analytic solution (dotted) and LES simulations (solid lines). Simulations are shown until the cloud dissipated for the largest Bowen Ratio, i.e. until 0800 LST, because the analytic model is not valid in clear conditions. Inversion height, z_i, is plotted for (a) $\beta = \{0.1, 0.3\}$ and (b) $\beta = \{1, 2\}$. Cloud thickness, h, is plotted for (c) $\beta = \{0.1, 0.3\}$ and (d) $\beta = \{1, 2\}$. Cloud thickness was also calculated using LCL for the $\beta = 0.1$ and $\beta = 2$ cases (dashed). The vertical dashed lines mark sunrise.

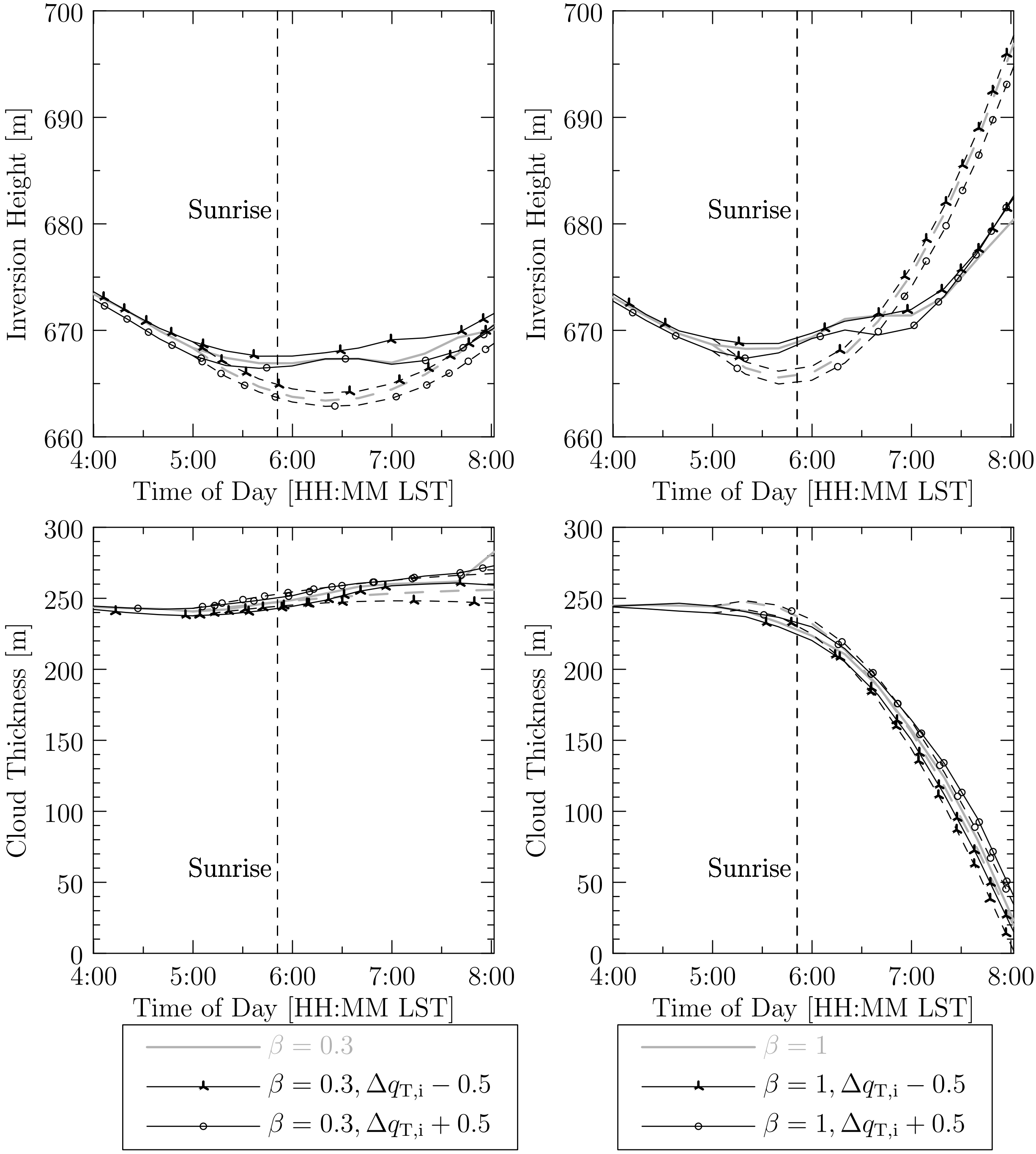

FIG. 6. Sensitivity of inversion height (top), and cloud thickness (bottom) to total moisture jump at the inversion and initial cloud base height, computed by the analytic solution (dashed) and the LES simulation (solid lines). Results for Bowen Ratios of 0.3 (left) and 1 (right) are shown. The original total moisture jump is colored gray, reduced case is marked with triangle and the increased case is marked with a circle.

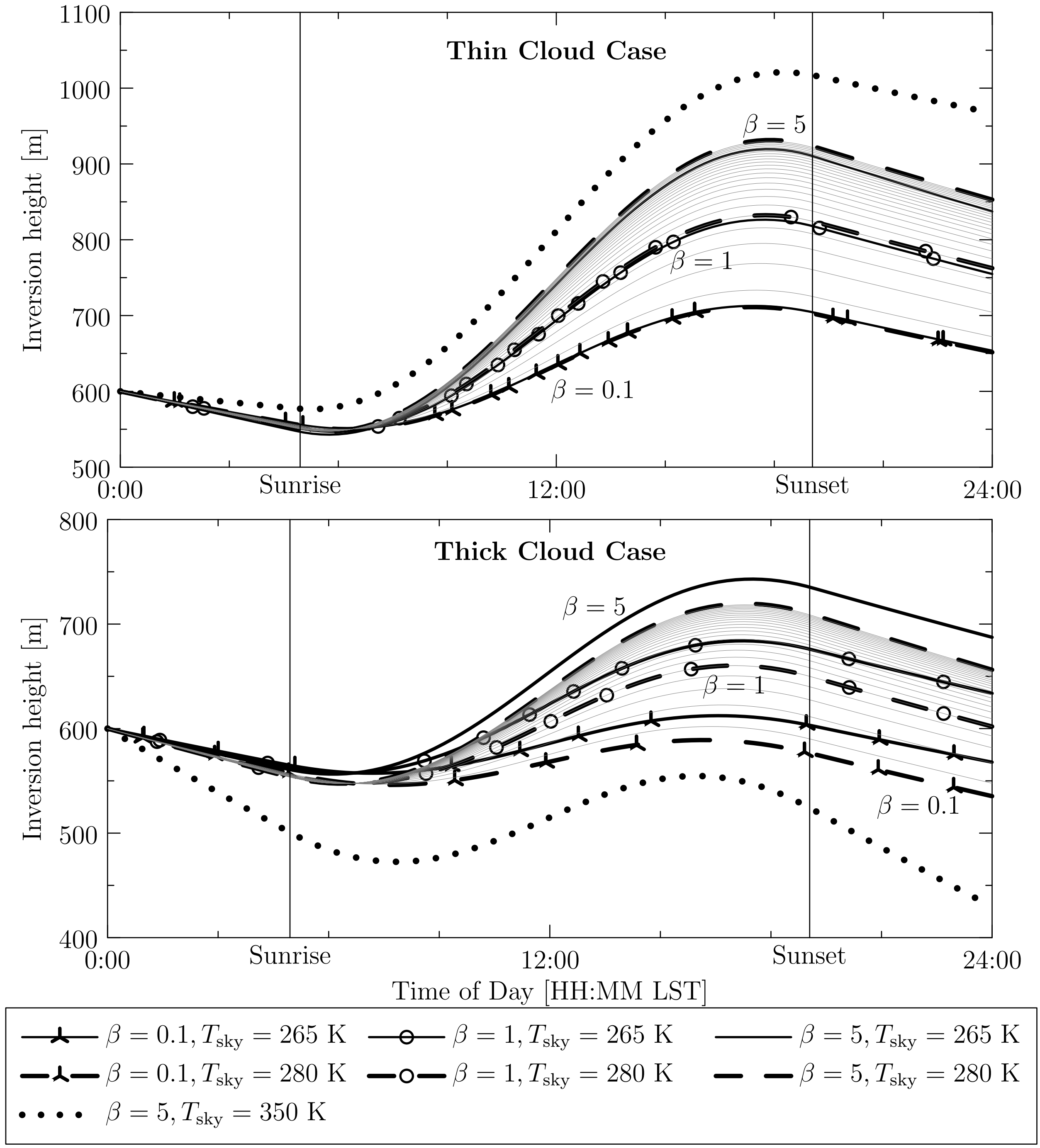

FIG. 7. Inversion height trend ($z_{\mathrm{i}}(t)$) with respect to different Bowen Ratios and cloud top temperatures for the thin cloud case ($[0, 200]$ m, top) and the thick cloud case ($[200, 400]$ m, bottom). Other variables are fixed at $\mathrm{T_{srf}} = 289$ K, $\mathrm{T_{cld}} = 285$ K, $\zeta_D = 51$ K, $D = -3.75 \times 10^{-6}$ s^{-1}. Simulations with $\mathrm{T_{sky}} = 265$ K (solid) and $\mathrm{T_{sky}} = 280$ K (dashed) are shown. Simulations for Bowen Ratios between 0.1 and 5 are shown as thin gray lines for the $\mathrm{T_{sky}} = 280$ K case with 0.2 increments. The dotted line is an admittedly unrealistic parameter choice to show a case where $z_{\mathrm{i}}(t)$ decreases. For this and all future graphs a latitude equal to 32.85° N and Julian day of 196 were used for solar zenith angle calculations.

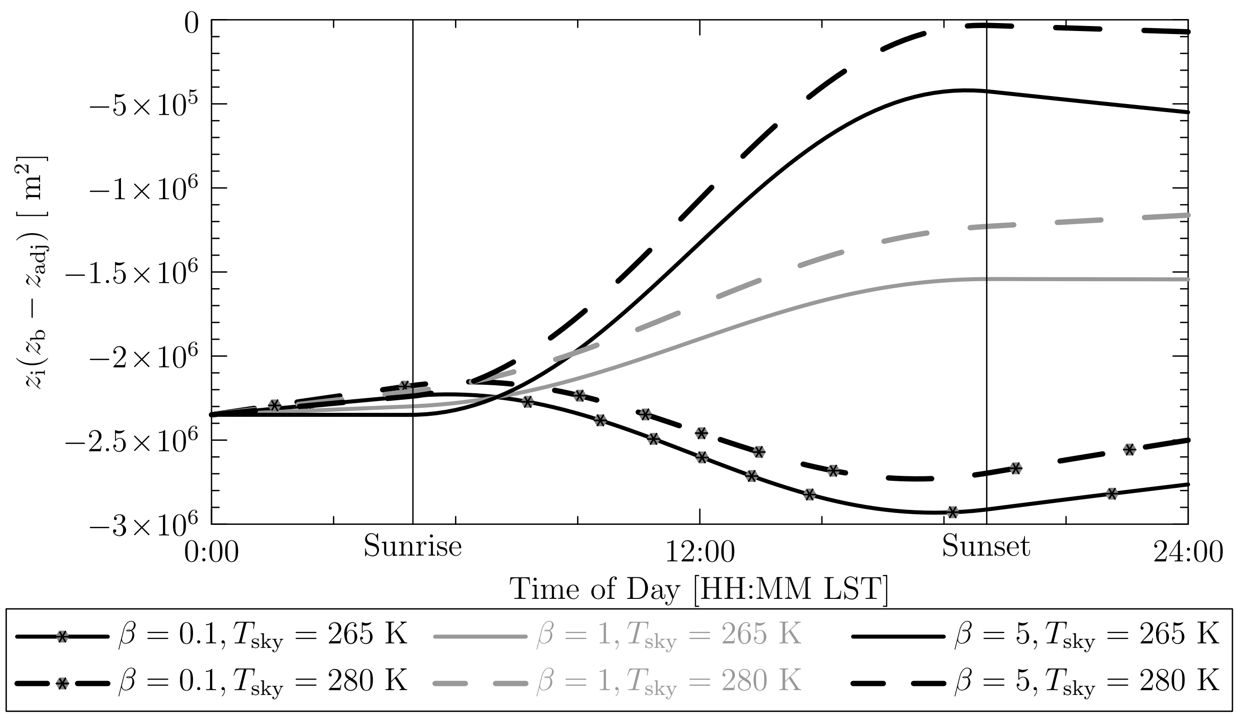

FIG. 8. $z_i(z_b - z_{adj})$ (proxy for cloud base height) timeseries for different Bowen Ratios and cloud top temperatures. Cases for $T_{sky} = 265$ K (solid) and $T_{sky} = 280$ K (dashed) are shown. Other variables are fixed at $T_{srf} = 289$ K, $T_{cld} = 285$ K, $\zeta_D = 51$ K, $D = -3.75 \times 10^{-6}$ s^{-1}.

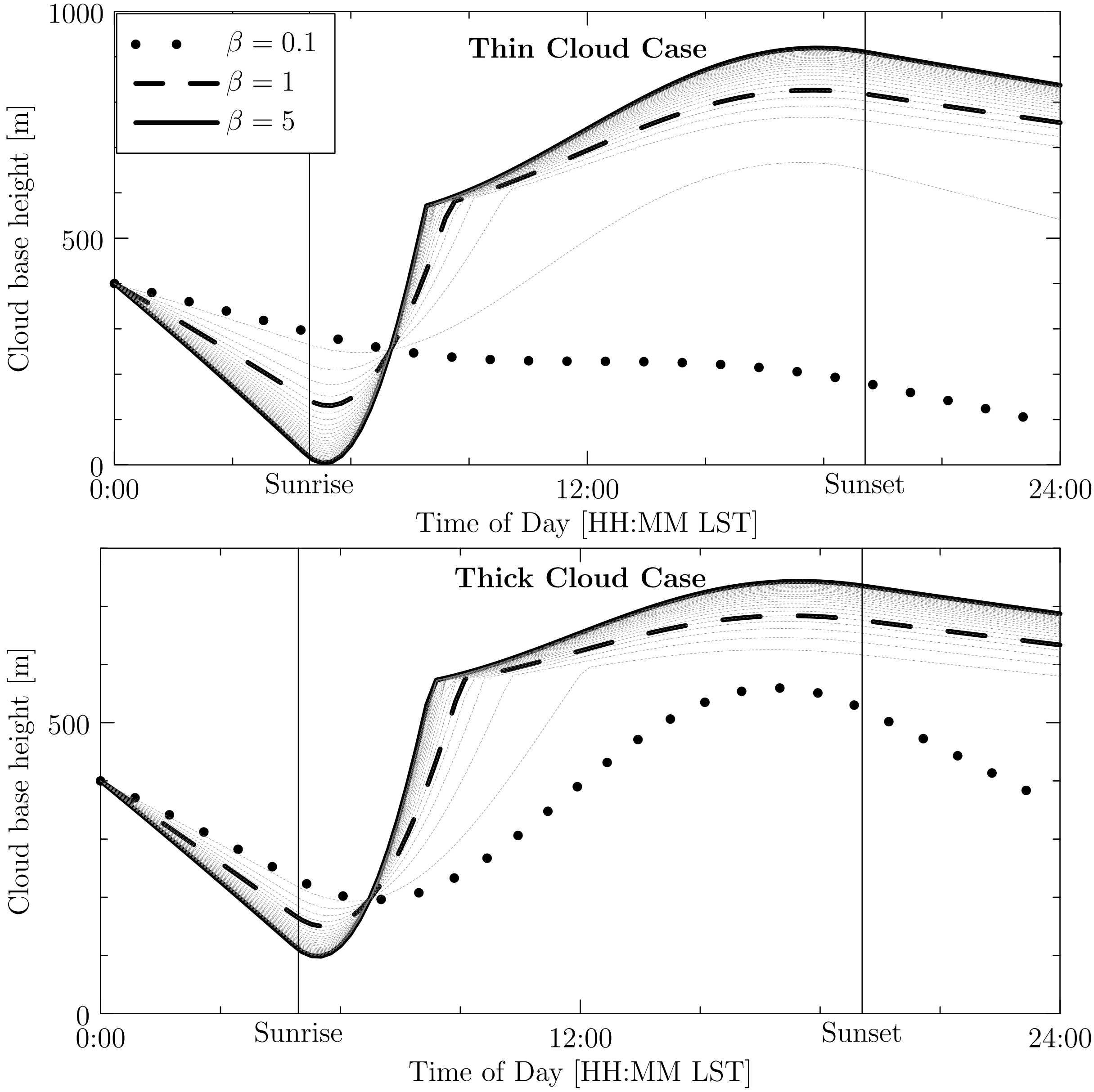

FIG. 9. Cloud Base Height timeseries ($z_b(t)$) for different Bowen Ratios for the thin cloud case ($[0, 200]$ m, top) and the thick cloud case ($[200, 400]$ m, bottom). The kink in the line occurs when the cloud base height reaches the inversion height. The thin gray lines represent Bowen Ratios from 0.1 to 5 with 0.2 increments. Other variables are fixed at $T_{srf} = 289$ K, $T_{cld} = 285$ K, $\zeta_D = 51, D = -3.75 \times 10^{-6}$ s^{-1}, $z_{adj} = 1600$ m, $z_i(0) = 600$ m, $T_{sky} = 265$ K.

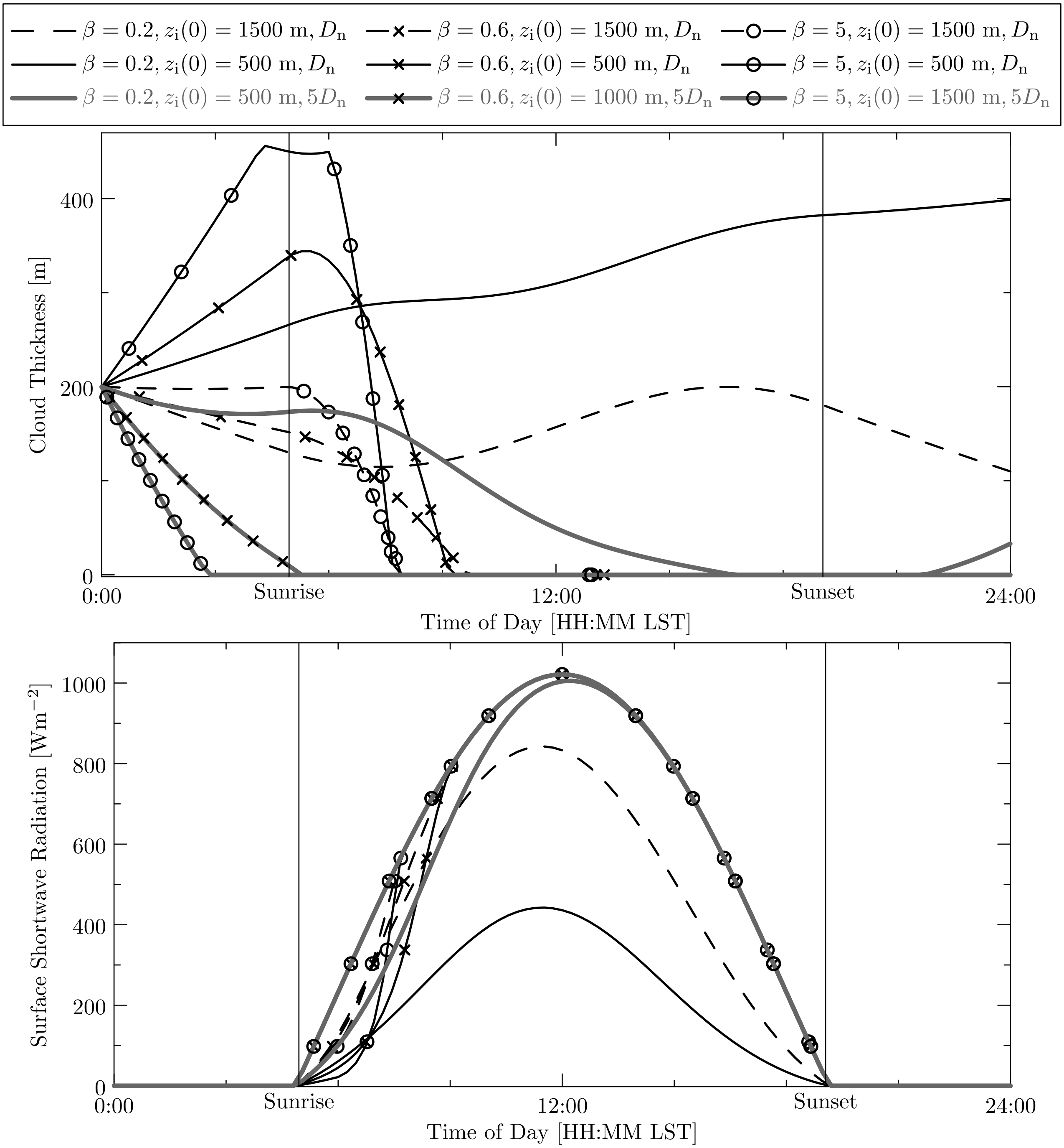

FIG. 10. Cloud thickness evolution (top) and resulting surface shortwave radiative fluxes (bottom) for different Bowen Ratios, initial inversion heights, and subsidence values. High initial inversion height cases of $z_i = 1500$ m are represented by dashed lines, $z_i = 500$ m cases are represented by solid lines and high subsidence cases are represented by thick lines. $D_n = -3.75 \times 10^{-6}\ \mathrm{s}^{-1}, \mathrm{T_{srf}} = 289$ K$, \mathrm{T_{cld}} = 285$ K$, \mathrm{T_{sky}} = 270$ K$, \zeta_D = 51$ K$, \Delta q_{\mathrm{T,i}} = -10$ g kg$^{-1}, \Delta\theta_{\mathrm{l,i}} = 10$ K.

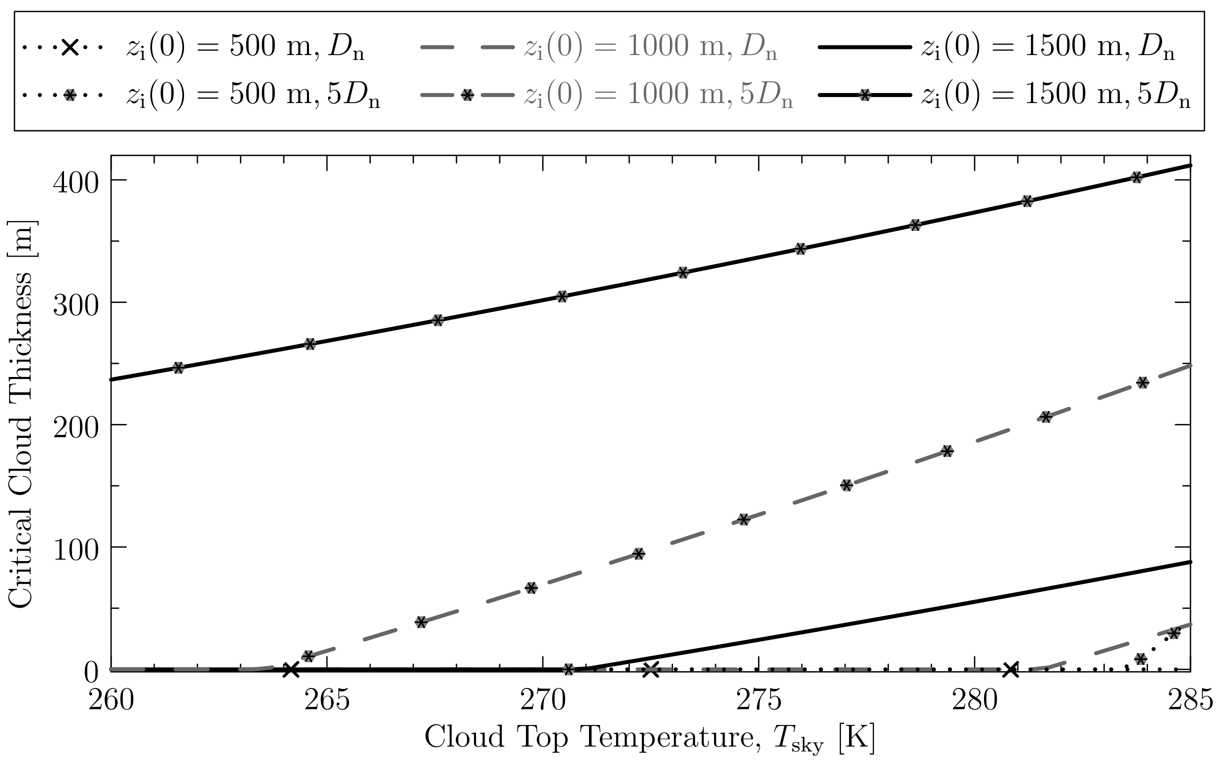

FIG. 11. Maximum cloud thickness that can be dissipated by sunrise for different cloud top temperatures, initial inversion heights and subsidence values. For normal subsidence values of D_n, only a very thin cloud dissipates for the $z_i(0) = 1000$ m and $z_i(0) = 1500$ m cases. A zero result means that the cloud will not dissipate before sunrise for the given conditions. $D_n = -3.75 \times 10^{-6}$ s^{-1}. Other variables are fixed at $\beta = 1, T_{srf} = 289$ K, $T_{cld} = 285$ K, $\zeta_D = 51$ K.

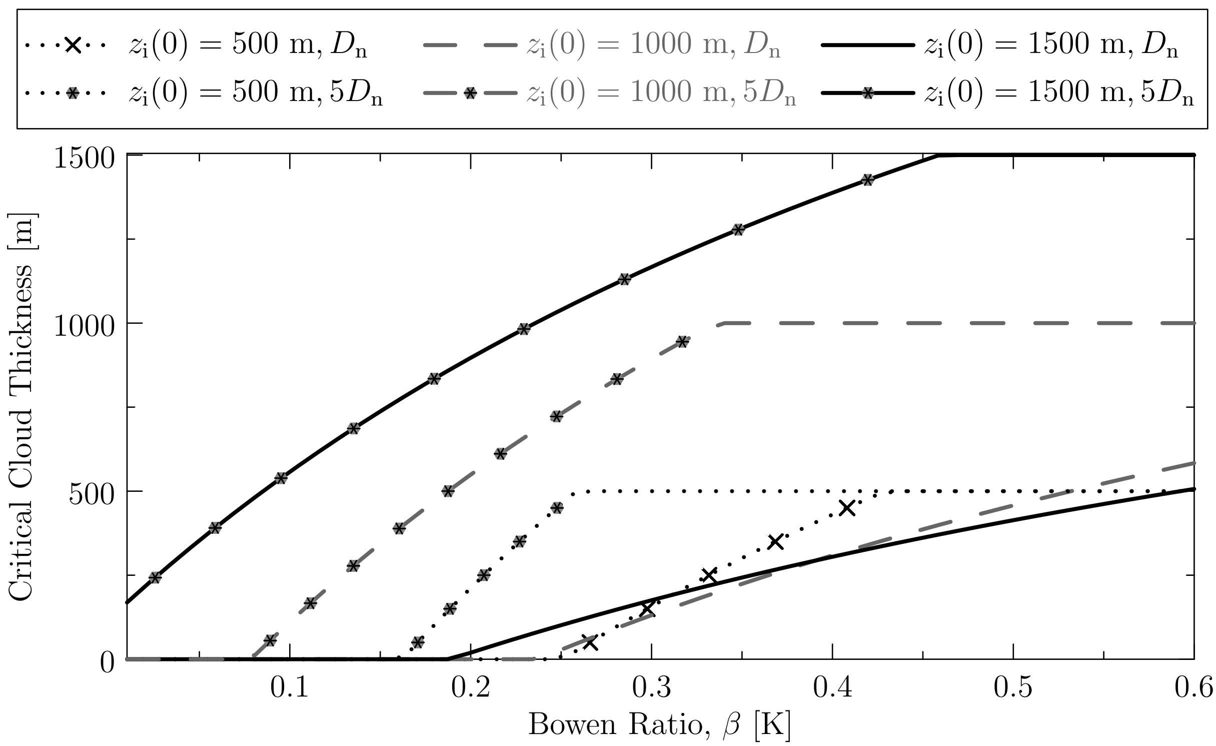

FIG. 12. Maximum cloud thickness that can be dissipated by sunset for different Bowen Ratios, initial inversion heights and subsidence values. A zero result means that the cloud will not dissipate before sunset for the given conditions. Horizontal lines result when the "dissipatable" cloud thickness reaches the initial inversion height. Parameters are $D_n = -3.75 \times 10^{-6}$ s^{-1}, $T_{srf} = 289$ K, $T_{cld} = 285$ K, $T_{sky} = 270$ K, $\zeta_D = 51$ K, $\Delta q_{T,i} = -5$ g kg^{-1}, $\Delta\theta_{l,i} = 10$ K, $\Delta\theta_{v,i} = 10$ K.

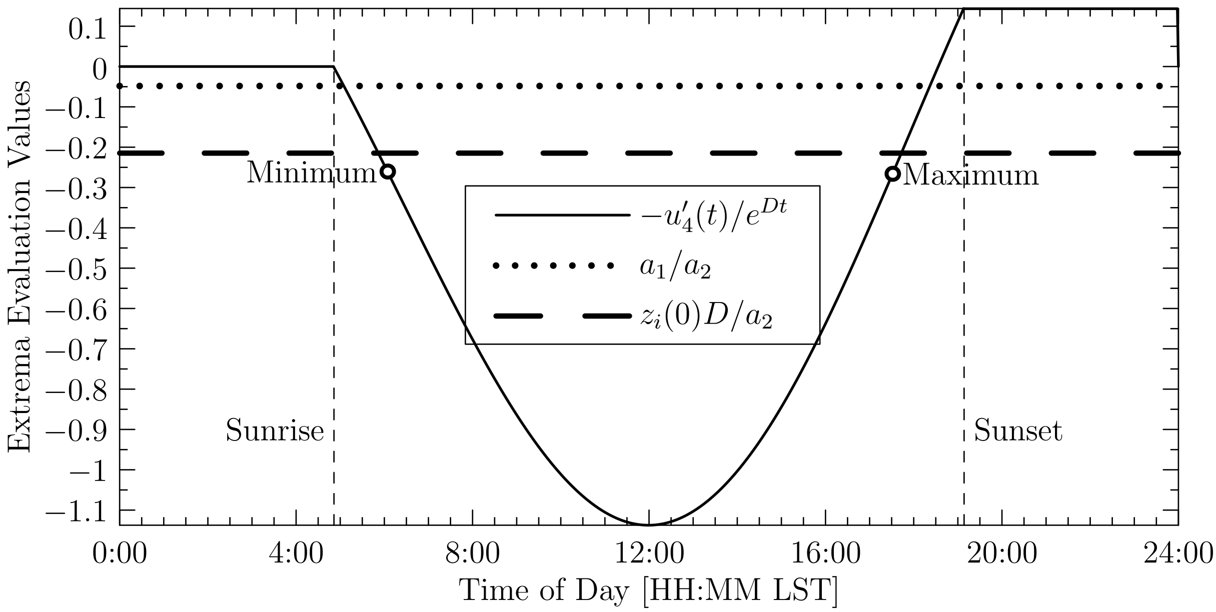

FIG. 13. Evaluation of the terms in Eq. (101) to find the inversion height extrema points.

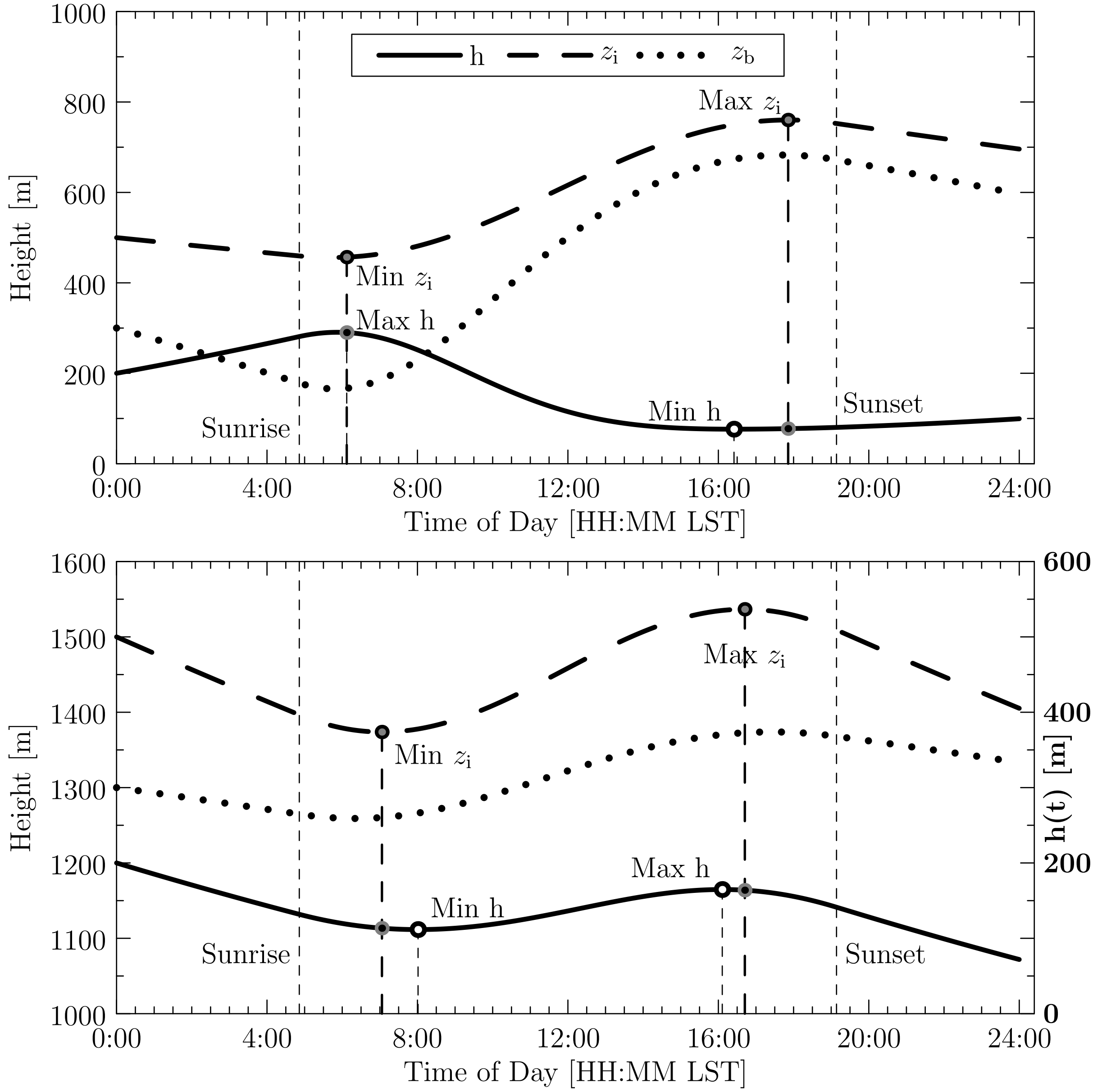

FIG. 14. Evaluation of the cloud thickness and its extrema values. Both cases have an initial cloud thickness of 200 m, but the top figure has $z_i(0) = 500$ m and the bottom figure has $z_i(0) = 1500$ m. The remaining parameters are the same, i.e. $\beta = 0.2, T_{srf} = 289$ K$, T_{cld} = 285$ K$, T_{sky} = 270$ K$, \zeta_D = 51$ K.

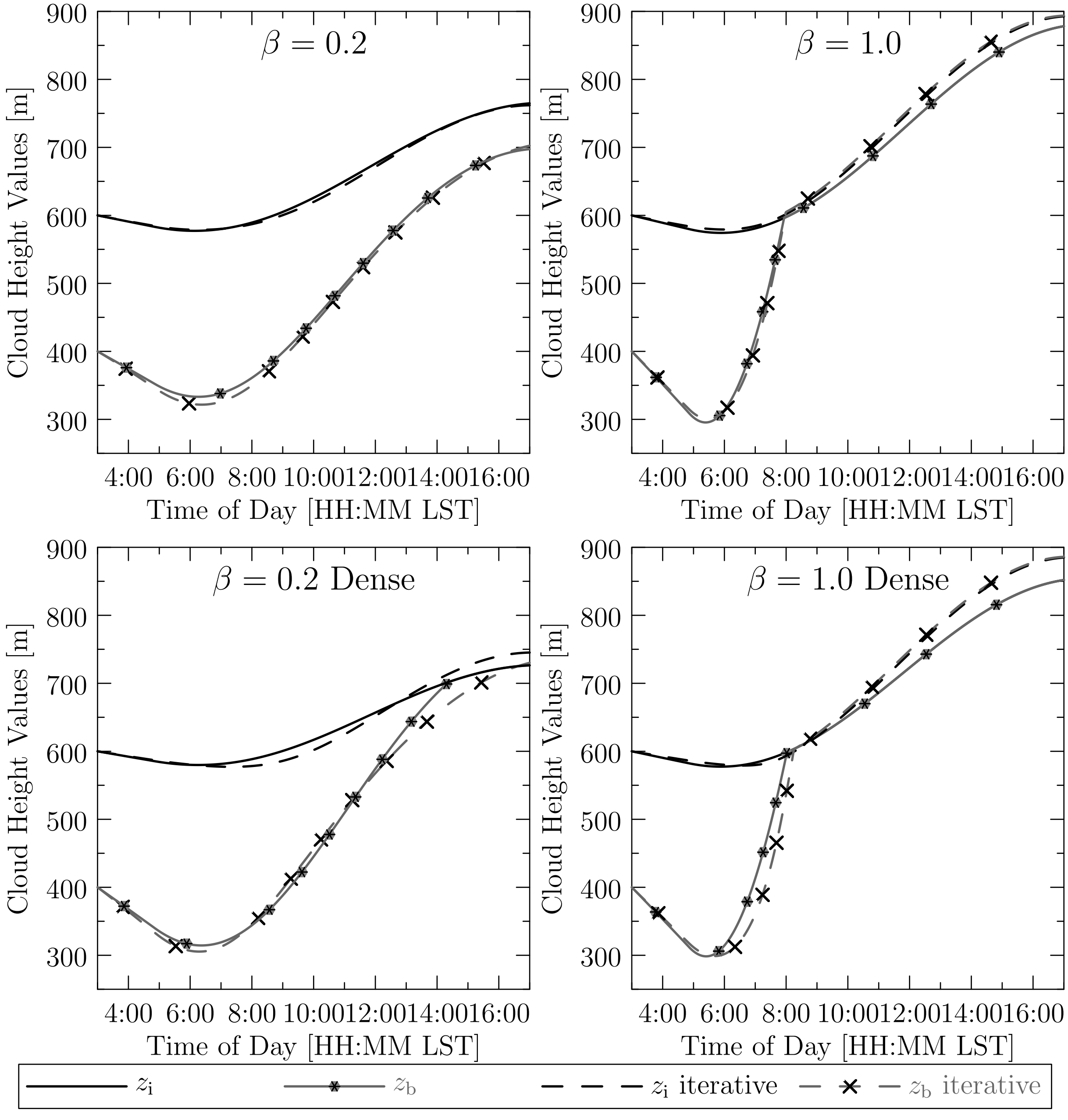

Fig. B1. The constant optical depth solution (solid) follows the iterative optical depth solution (dashed) closely, showing that our constant optical depth assumption is valid. $\Gamma_l = 5 \times 10^{-7}$ m^{-1} for the normal case, and $\Gamma_l = 10^{-7}$ m^{-1} for the dense case. Rest of the simulation parameters are $z_i(0) = 600$ m, $z_b(0) = 400$ m, $T_{srf} = 289$ K, $T_{cld} = 285$ K, $T_{sky} = 265$ K, $D = -3.75 \times 10^{-6}$ s^{-1}.